CrossMark

RESEARCH ARTICLE

# Pore pressure embrittlement in a volcanic edifice

Jamie Farquharson[1] · Michael J. Heap[1] · Patrick Baud[1] · Thierry Reuschlé[1] ·
Nick R. Varley[2]

**Abstract** The failure mode of porous rock in compression—dilatant or compactant—is largely governed by the overlying lithostatic pressure and the pressure of pore fluids within the rock (Wong, Solid Earth 102:3009–3025, 1997), both of which are subject to change in space and time within a volcanic edifice. While lithostatic pressure will tend to increase monotonously with depth due to the progressive accumulation of erupted products, pore pressures are prone to fluctuations (during periods of volcanic unrest, for example). An increase in pore fluid pressure can result in rock fracture, even at depths where the lithostatic pressure would otherwise preclude such dilatant behaviour—a process termed pore fluid-induced embrittlement. We explore this phenomenon through a series of targeted triaxial experiments on typical edifice-forming andesites (from Volcán de Colima, Mexico). We first show that increasing pore pressure over a range of timescales (on the order of 1 min to 1 day) can culminate in brittle failure of otherwise intact rock. Irrespective of the pore pressure increase rate, we record comparable accelerations in acoustic emission and strain prior to macroscopic failure. We further show that oscillating pore fluid pressures can cause iterative and cumulative damage, ultimately resulting in brittle failure under relatively low effective mean stress conditions. We find that macroscopic failure occurs once a critical threshold of damage is surpassed, suggesting that only small increases in pore pressure may be necessary to trigger failure in previously damaged rocks. Finally, we observe that inelastic compaction of volcanic rock (as we may expect in much of the deep edifice) can be overprinted by shear fractures due to this mechanism of embrittlement. Pore fluid-induced embrittlement of edifice rock during volcanic unrest is anticipated to be highest closer to the conduit and, as a result, may assist in the development of a fractured halo zone surrounding the conduit, potentially explaining commonly observed near-conduit outgassing at many active volcanoes. Further, rock embrittlement at depth may create transient outgassing pathways by linking fracture networks near the edifice to larger-scale regional fault systems. Our experimental results affirm that pore pressure fluctuations associated with volcanic unrest may play a crucial role in dictating the evolution of a volcanic system.

**Keywords** Andesite · Mechanical deformation · Pore pressure · Brittle, inelastic compaction · Volcanic edifice · Volcán de Colima

✉ Jamie Farquharson
farquharson@unistra.fr

[1] Laboratoire de Déformation des Roches, Équipe de Géophysique Expérimentale, Institut de Physique de Globe de Strasbourg (UMR 7516 CNRS, Université de Strasbourg/EOST), 5 rue René Descartes, 67084 Strasbourg cedex, France

[2] Facultad de Ciencias, University of Colima, Colima 28045, Mexico

## Introduction

The capacity for magma to exsolve volatiles and outgas during ascent through a volcanic conduit or dyke exerts a crucial influence on the style, magnitude, and duration of volcanic eruptions (e.g. Jaupart 1998; Edmonds et al. 2003; Taisne and Juapart 2008). Efficiently outgassed magmas are often erupted in effusive events which, despite their ability to cause substantial and permanent infrastructural and property damage, are generally non-fatal (e.g. Auker et al. 2013). In contrast, magmas which

cannot outgas sufficiently will be oversaturated in volatiles, potentially resulting in the buildup of pressure and catastrophic explosive eruptions (e.g. Melnik et al. 2005; Diller et al. 2006). Thus, the potential for outgassing through the conduit (e.g. Edmonds et al. 2003; Nicholson et al. 2013; Plail et al. 2014; Shields et al. 2014), through a fractured zone around the conduit (e.g. Rust et al. 2004; Lavallée et al. 2013; Gaunt et al. 2014), and into the edifice host rock (e.g. Jaupart 1998) are all important considerations with respect to the volatile budget of a volcano, and the attendant implications for eruptive behaviour. Research into edifice rock deformation is therefore required to improve our understanding of the mechanisms underpinning the style and dynamics of volcanic eruptions.

It has long been acknowledged that pore fluids and pore fluid pressure have a significant function in faulting processes (Hubbert and Rubey 1959; Rubey and Hubbert 1959; Johnson and McEvilly 1995; Baud et al. 2000; Faulkner and Rutter 2001; Vinciguerra et al. 2004; Paterson and Wong 2005; Ougier-Simonin and Zhu 2013) and slope stability, usually in the context of mass movement and slope failure (e.g. Day 1996; Voight and Elsworth 1997; Donnadieu et al. 2001; Jousset et al. 2013). The mechanical behaviour and failure mode of rocks are governed by their physical properties (such as porosity and pore size) and the local the effective pressure ($P_{eff}$) (e.g. Wong and Baud 2012). The effective pressure acting on a rock is a function of the confining pressure (equivalent to the lithostatic pressure) surrounding it, and the pore fluid pressure within it ($P_c$ and $P_p$, respectively). Inelastic strain accumulation at low effective pressure often results in dilatant failure (macroscopically "brittle" behaviour, i.e. fracture generation), whereas a compactant failure mode—where the deforming material experiences inelastic porosity loss during deformation—is typically observed at high effective pressures (e.g. Wong and Baud 2012). Both of these failure modes have been observed in previous experimental studies on volcanic rocks in which the pore fluid pressure was kept constant and experiments were performed at different confining pressures (e.g. Kennedy et al. 2009; Zhu et al. 2011; Loaiza et al. 2012; Adelinet et al. 2013; Heap et al. 2014a, 2015a, c). However, the effective pressure will decrease if pore pressure increases and therefore rock embrittlement—the transition from an elastic or compactant regime to dilatant (i.e. macroscopically brittle) failure—can occur if the pore pressure is increased sufficiently.

In a volcanological context, deviations from the equilibrium pore pressure have been thought responsible for the mechanical deformation of volcanic edifices (e.g. Nishi et al. 1996; Caricchi et al. 2011; Jousset et al. 2013; Sisson and Power 2013). Within a volcanic system, edifice rocks are typically fluid-saturated (Day 1996). This multiphase medium is often subject to significant thermal and mechanical stresses (e.g. Roman et al. 2004; Costa et al. 2007) which offer a range of processes by which pore fluid pressure may increase. For example, source vents of explosive eruptions are often plugged by variably fractured lava domes or choked conduits (e.g. Voight et al. 1999; Johnson and Lees 2000; Diller et al. 2006). As long as volatile disequilibrium exists, a gas phase will continue to exsolve from the magma, allowing pore pressure to build beneath the plug (Lensky et al. 2004). Further, solidification or crystallisation of conduit magma, thermal expansion of fluids, and hydrothermal circulation can all affect edifice pore fluid volume in an open system (e.g. Voight and Elsworth 1997; Sisson and Bacon 1999); as such, we suggest that sustained increases in pore pressure are probably a common occurrence within the edifice of a volcanic system. The cyclic or episodic nature of many volcanic processes is similarly well documented: cycles in outgassing, seismicity, and explosive eruptions have been detected at numerous volcanic systems, often reflected in contemporaneous geophysical data, highlighting the inflation and deflation of the edifice (Denlinger and Hoblitt 1999; Watson et al. 2000; Michaut et al. 2013; Yokoo et al. 2013; Anderson et al. 2015; Heimisson et al. 2015). This fact is significant, as it suggests that cyclic processes in the conduit, such as the movement of gas aggregates or "slugs" (James et al. 2004; De Lauro et al. 2012), the ascent of vesicularity-stratified magma (Voight et al. 1999), or transient plugging events (Johnson and Lees 2000), may bring about oscillatory volumetric deformation of the edifice. Correspondingly, we may expect oscillation of pore fluid pressures in the edifice over a range of timescales.

## Evidence for deviations in edifice pore fluid pressure

Direct field evidence for magmagenic fluctuations in pore fluid pressure is rare, but does exist. For example, two magma intrusion events at Krafla, Iceland (September 1977 and July 1978), were associated with transient increases in country rock pore pressure measured at a proximal geothermal well. During the first event, an increase of 0.76 MPa was recorded (4300 m from the intrusion); during the latter, an increase of 0.36 MPa was recorded approximately 9300 m from the intrusion (Sigurdsson 1982; Elsworth and Voight 1992; Elsworth et al. 1996). Shibata and Akita (2001) report water level changes in wells proximal to Usu Volcano, Japan, interpreted as a direct result of volumetric expansion of the magma chamber, and subsequent intrusion of magma into the edificial fracture network. A similar interpretation is used to explain water pressure changes measured near Kīlauea, Hawai'i (Hurwitz and Johnson 2003). Hydraulic head changes of a few centimetres in these latter examples reflect transient pore pressure increases on the order of 0.001 MPa

(hydraulic head is directly related to the pressure head $\psi$, which in a confined well can be described by $\psi = P_p/\rho_f g$, where $\rho_f$ and $g$ are the fluid density and acceleration due to gravity, respectively). Further quantitative and qualitative examples are highlighted by Newhall et al. (2001), who estimate that pore fluid pressures in confined volcanic systems may rise by as much as several tens of megapascal as a result of magmagenic thermomechanical pressurisation. Further, hydrofractures—where the pore fluid pressure exceeds the confining pressure and results in brittle failure of rock—have also been inferred in volcanic systems from field observations and chemical analysis (e.g. Heiken et al. 1988; Gudmundsson et al. 2008), a testament to the high pore fluid pressures that can accumulate in rock adjacent to the conduit and intrusions.

As magmatic intrusions and ascent comprise the predominant source of thermal and mechanical stresses within a volcanic structure, thus, we expect the rates and magnitudes of increases in pore pressure, and their impact on rock mechanical behaviour and failure mode, to be correspondingly highest near to the conduit and intrusive magmatic bodies (for example, pore fluid pressure has been estimated to increase with temperature at a rate of around 1–2 MPa°C$^{-1}$: Knapp and Knight 1977). Indeed, recent work (e.g. Rust et al. 2004; Lavallée et al. 2013; Gaunt et al. 2014) has argued the existence of a "halo" surrounding the conduit that comprises intensely fractured magma or edifice rock, through which magmatic gases—primarily steam—can readily outgas. Strain modelling (Young and Gottsmann 2015) indicates that this assumption is necessary to explain recent syneruptive volumetric strain data recorded at Soufrière Hills Volcano (Montserrat). Further, a recent study by Strehlow et al. (2015) employs finite element analysis to model the poroelastic responses of a saturated volcanic edifice system to subsurface magmagenic strain. These studies emphasise the importance of understanding the hydromechanical interactions between the porous edifice and magma chambers, conduits, and intrusions.

Field evidence from Volcán de Colima illustrates that subsurface magmagenic strain is reflected in the degree of fumarolic outgassing from the upper flanks of the edifice. Figure 1 shows previously unpublished thermal emission data along a transect on the upper edifice of the volcano, for three dates with varying volcanic activity. Airborne thermal surveillance has previously proved to be a useful tool to establish variations in the emplacement of domes at Volcán de Colima, as well as variations in fumarole temperature and heat flux (Hutchison et al. 2013), whilst the monitoring of fumarole temperatures from fixed ground vantage points has also contributed in the understanding of the evolution of eruptive activity (Stevenson and Varley 2008). In Fig. 1, we infer peaks above the background temperature (in the range of 0–20 °C) to represent fumarole emission. Notably, during a period of minimal eruptive activity—July 2012—just one active emitting fumarole

was registered in the transect. In January 2013, effusive activity was occurring, but extruding at a low rate and confined within a deep crater. The increase in activity relative to July 2012 is evident in the appearance of a second fumarole, at a greater distance from the crater rim. Finally, the high-temperature fumaroles observed in February 2015 reflect higher rates of extrusion and correspondingly more vigorous outgassing from the flanks of the volcano. Thus, we can correlate the ascent of strain-inducing bodies (gas or magma) with increases in gas flux from the edifice (e.g. Harris and Maciejewski 2000), in turn associated with increases in pore fluid pressure.

Distal from volcanic conduits, larger-scale regional fault systems have also been observed to vent magmatic gases (e.g. Heiligmann et al. 1997; Giammanco et al. 1998). A study by Varley and Taran (2003) showed that fault architecture near Volcán de Colima did not comprise a constant pathway for magmatic gas species. However, anomalous radon (Varley and Taran 2003) and boron (Taran et al. 2000) measurements around the edifice could suggest that transient pathways are formed at some depth, temporarily allowing gases to escape from the volcanic system. Further, long-period (LP) seismic events, characterised by transient seismic signals lasting tens of seconds with periods less than or equal to two seconds (Lahr et al. 1994; Chouet 1996; Neuberg 2000), have been recorded in abundance in many volcanic environments, such as Volcán de Colima, Mexico (e.g. De Lauro et al. 2012; Boué et al. 2015), and Merapi, Indonesia (e.g. Jousset et al. 2013). LP events have been interpreted as shear fracture events (e.g. Neuberg et al. 2006; Varley et al. 2010; Thomas and Neuberg 2012), slow-rupture failure of edifice-forming material (e.g. Harrington and Brodsky 2007; Bean et al. 2014), or the resonance of fluid-filled fractures (Lahr et al. 1994; De Lauro et al. 2012).

Despite the evidence described above, there is a paucity of experimental studies on the impact of fluctuating pore fluid pressures on the mechanical behaviour and failure mode of volcanic rocks, and the attendant implications for outgassing and volcanic edifice stability. For example, the potential for the existence of fractures in deeper parts of the edifice—where we would expect predominantly compactant behaviour (Heap et al. 2015a)—means that there must be a mechanism of embrittlement which can occur under stress conditions which would otherwise preclude brittle behaviour. We present herein an experimental study designed to investigate the process of pore fluid-induced embrittlement in porous volcanic rocks.

## Materials and methods

Our samples were taken from a block of porous andesite (block C8, as described in Heap et al. 2014a, 2015a) collected from the 1998 block-and-ash flow deposits of Volcán de
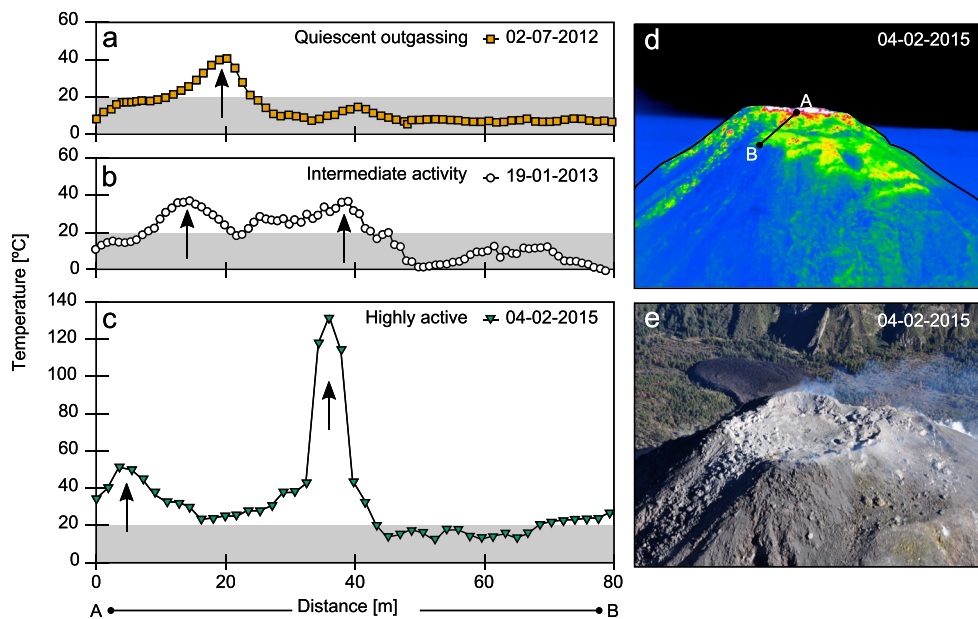
**Fig. 1** Temperature recorded along a transect from the crater rim of Volcán de Colima down the uppermost part of the edifice (i.e. parallel to the principal slope direction) using a Jenoptik VarioCam with 640 × 480 pixel resolution (sensitive in the 7.5–14 μm wavelength band). Data were acquired from light aircraft overflights of the volcano on three dates: **a** 02 July 2013, **b** 19 January 2013, and **c** 04 February 2015. Flights were in the early morning in each case, in order to avoid the effects of solar heating, and surface features were used in order to ensure consistency of viewing geometry, pixel size, and field of view. Each time period corresponds to a different level of effusive activity. *Arrows* highlight peaks above the average background temperature range, indicating the presence of fumaroles. Panel **d** shows the transect on a typical thermal image, and **e** is a true-colour photograph from approximately the same vantage

Colima. Situated in the Trans-Mexican volcanic belt, this andesitic stratovolcano is one of the most active volcanoes in North America, regularly producing both effusive and explosive products (e.g. Varley et al. 2010; James and Varley 2012). Although the material was collected from Volcán de Colima, the attendant discussions and conclusions are more widely applicable to stratovolcanoes with comparable eruption styles and cycles, such as Soufrière Hills Volcano (Montserrat), Lascar (Chile), Ruapehu (New Zealand), or Merapi (Indonesia). Right cylinders were cored from the block, with a diameter of 20 mm and a nominal length (precision-ground) of 40 mm. The block contains $59.9 \pm 1.0$ wt% $SiO_2$ (determined by X-ray fluorescence, see Heap et al. 2014a) and is thus representative of historical eruptive products (Luhr 2002; Savov et al. 2008). C8 andesite contains a high phenocrystal fraction (over 0.5: estimated through image analysis of scanning electron microscope photomicrographs), comprising plagioclase, clinopyroxene, and orthopyroxene within a glassy and microlitic groundmass. A subsample of nine cores was selected in order to minimise variations in connected (water) porosity ($\phi$), which ranges from 0.16 to 0.18, determined using the triple-weight Archimedes method (see Guéguen and Palciauskas 1994).

Prior to all deformation experiments, samples were vacuum saturated with distilled water. For the triaxial experiments, a simple effective pressure law is used, whereby $P_{eff} = P_c - \alpha P_p$, where $\alpha$ is the Biot-Willis coefficient, a poroelastic constant assumed herein to be equal to 1. Whilst we acknowledge that

$\alpha$ could be slightly <1 for our andesite (see Appendix A), for the relatively small range of effective pressures imposed in this study, the effect of $\alpha \neq 1$ is negligible and inconsequential in terms of our discussion. Confining and pore pressures were increased slowly, to ensure the sample suffered no damage, and were not subjected to an effective pressure above that targeted for each given experiment. In each test, the samples were left in the triaxial press overnight, so as to achieve microstructural equilibrium prior to deformation.

Other than in extreme proximity to the conduit, host rock in a volcano will rarely be above the glass transition temperature of its melt phase. Whilst we acknowledge that some processes and mechanisms will be enhanced even at temperatures below this threshold (such as subcritical crack growth: Brantut et al. 2013), all our tests were carried out at room temperature. Given that Volcán de Colima summits around 3850 m a.s.l. (Mueller et al. 2013), our experiments were performed at confining pressures between 0 and 40 MPa (Table 1). The bulk density $\rho_b$ of volcanic rock at Volcán de Colima has been observed to vary significantly (e.g. Mueller et al. 2011; Farquharson et al. 2015; Lavallée et al. 2016), the majority of erupted products falling in a density range between around 2000 and 2500 kg m$^{-3}$ (Heap et al. 2015a; Lavallée et al. 2016). Lithostatic pressure can be approximated by $\rho_b g z$, where $g$ and $z$ are acceleration due to gravity and depth, respectively. Accordingly, the imposed pressures used throughout this study are well within a volcanically relevant pressure

**Table 1** Summary of experimental conditions and results. $P_c$, $P_p$, and $P_{eff}$ are confining, pore, and effective pressures, respectively. $\sigma_P$ is the peak stress of brittle failure samples; $C'$ is the onset of dilatant microcracking; $C^*$ is the onset of shear-enhanced compaction

| Sample | Porosity | $P_c$ [MPa] | Initial $P_p$ [MPa] | $P_p$ increase rate [MPa s$^{-1}$] | $P_{eff}$ at failure [MPa] | $\sigma_P$ [MPa] | $C'$ [MPa] | $C^*$ [MPa] |
|---|---|---|---|---|---|---|---|---|
| C8 29 | 0.16 | 0 | 0 | – | 0 | 35.7 | 18.1 | – |
| C8 14 | 0.16 | 15 | 10 | – | 5 | 73.5 | 29.8 | – |
| C8 13 | 0.16 | 20 | 10 | – | 10 | 91.1 | 44.2 | – |
| C8 32 | 0.16 | 40 | 10 | – | 30 | – | – | 103.0 |
| C8 12 | 0.17 | 40 | 10 | $5.0 \times 10^{-1}$ | 0.4 | 60.0[a] | – | – |
| C8 03 | 0.16 | 40 | 10 | $5.0 \times 10^{-2}$ | 1.0 | 60.0[a] | – | – |
| C8 27 | 0.16 | 40 | 10 | $5.0 \times 10^{-3}$ | 1.3 | 60.0[a] | – | – |
| C8 28 | 0.16 | 40 | 10 | $5.0 \times 10^{-4}$ | 4.9 | 60.0[a] | – | – |
| C8 31 | 0.18 | 40 | 10 | $5.0 \times 10^{-3}$ | 12.4 | 60.0[a] | – | – |
| C8 34 | 0.16 | 40 | 10 | $5.0 \times 10^{-2}$ | 30 | – | – | 92.1 |

[a] Experiments were performed under load-control; differential stress $Q$ is maintained at 60 MPa throughout

domain, representing depths in the edifice from 0 m down to around 1600–2000 m.

Acoustic emissions (AE) during sample deformation are associated with microcracking (Lockner 1993). In order to assess microstructural damage, AE was monitored throughout the experiments with a piezoelectric transducer attached to the top of the upper piston, and the signal processed by AEwin software. AE energy is displayed herein in arbitrary units: AE hits were recorded if signal amplitude was greater than 40 dB; "energy" simply represents the root-mean-square of the received waveform. Note that we present these data in arbitrary units (root-mean-square of the waveform divided by $10^6$) as the values are not directly comparable with those recorded using different experimental or field setups: we use AE here as a tool to understand the onset and extent of microcracking during our experiments. Axial strain was measured using a displacement transducer mounted to the top of the axial piston and stress was monitored by a load cell. Confining and pore pressures were measured and regulated using servo-controlled actuators. See Heap et al. (2014b) for a schematic of the triaxial press.

Two types of test were performed: constant strain rate and constant differential stress experiments. For both types of experiment, the initial target confining and pore pressures were first applied to the sample (except in the case of the uniaxial experiment which was deformed in a water bath at atmospheric pressure). During the constant strain rate experiments, an axial load was applied at a constant strain rate of $10^{-5}$ s$^{-1}$ until the sample failed. During the tests, the pore and confining pressures were maintained constant by correcting for pressure excursions using two intensifiers (actuators); the recorded movement of the pore pressure actuator as it compensates for sample deformation yields the pore volume change (normalised to give the change in porosity $\Delta\phi$). As the initial porosity $\phi$ is known, we can thus monitor porosity during deformation (i.e. $\phi + \Delta\phi$). With increased differential stress,

a negative $\Delta\phi$ is indicative of compactant (porosity-reducing) behaviour, whereas $\Delta\phi > 0$ means that the behaviour is dilatant (porosity-increasing).

During the constant differential stress experiments, a constant differential stress $Q$ and confining pressure were maintained: following microstructural equilibration at the chosen effective pressure, the axial load was increased at a constant rate of $10^{-5}$ s$^{-1}$ until the differential stress was equal to 60 MPa (a value within the poroelastic domain, as guided by our previous constant strain rate tests). Samples were left overnight (for a minimum of 16 h) under constant differential stress. Since the rock is within the poroelastic domain, zero axial and volumetric deformation of the sample was recorded during this time. Pore pressures were then increased at servo-controlled rates ($5.0 \times 10^{-1}$, $5.0 \times 10^{-2}$, $5.0 \times 10^{-3}$, or $5.0 \times 10^{-4}$ MPa s$^{-1}$) from a starting value of 10 MPa. A further test was performed where a sample was held under a constant confining pressure and differential stress and the pore pressure was oscillated at regular intervals. In a final test, pore pressure was increased in a sample undergoing constant strain rate deformation in the compactant regime. Drainage in our experiments was assured at the implemented deformation and pore pressure increase rates by performing a supplementary experiment (see Appendix B), a consequence of the high initial porosity and permeability (around $3.0 \times 10^{-13}$ m$^2$: Heap et al. 2014a). All of the experiments reported in this study are summarised in Table 1.

## Results

### Constant strain rate with constant pore pressure

Figure 2a shows the stress-strain curves for each of the constant strain rate tests. A different behaviour can be observed
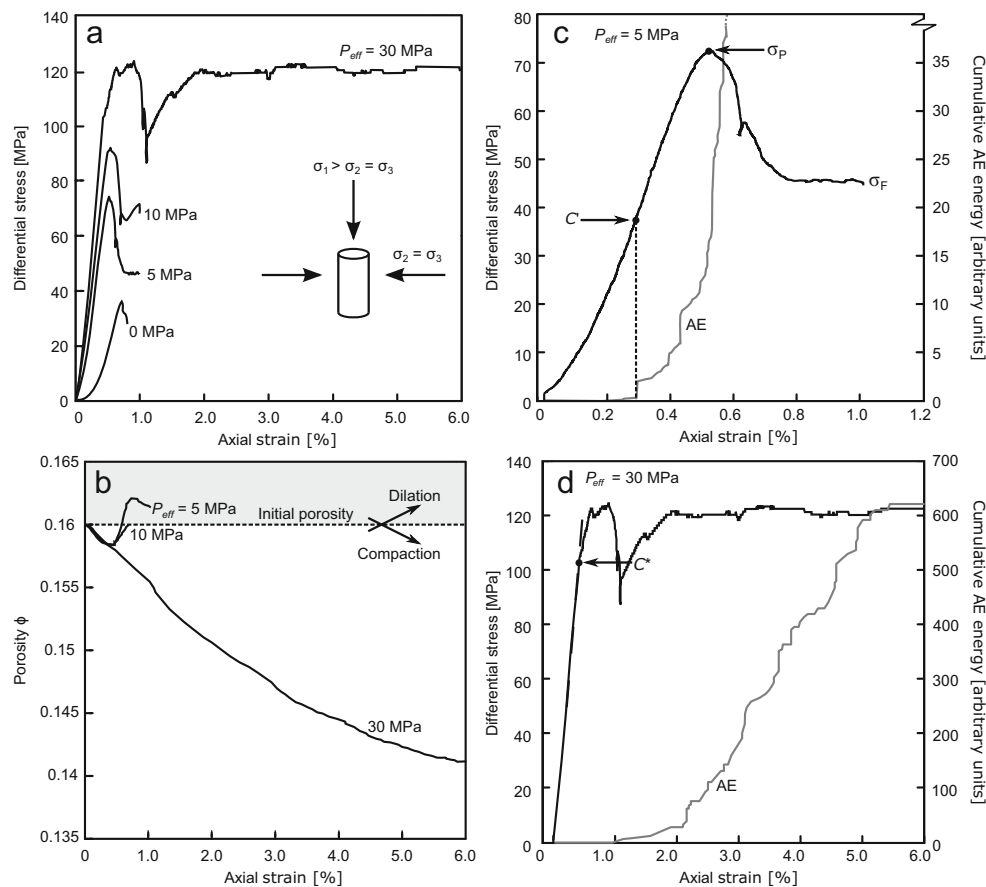
**Fig. 2** Mechanical data for andesites from Volcán de Colima deformed under a constant strain rate. Stress as a function of axial strain for all tests are shown in **a**. The orientations of the principal stresses ($\sigma_1$, $\sigma_2$, $\sigma_3$) are also shown with respect to our cylindrical samples. **b** The change in porosity during deformation for each sample from an initial value of $\phi = 0.16$ (except the uniaxial test, where this change cannot be monitored). **c** Example of a test where failure is in the brittle regime, in a sample deformed at an effective pressure of 5 MPa. Peak stress ($\sigma_P$) and residual post-failure stress ($\sigma_F$) are indicated, as is a threshold $C'$, which represents the onset of microcracking. Cumulative acoustic emission (AE) data are also shown, plotted in arbitrary units (refer to text for explanation). Note that the onset of AE in **c** corresponds with $C'$. Equivalent data are shown in **d** for a sample which failed through compaction (at an effective pressure of 30 MPa). In this case, failure is marked by $C^*$ (the onset of shear-enhanced compaction), the point where the stress-strain curve deviates from linear behaviour. This point is also associated with the onset of AE activity

for those deformed at effective pressures of 0, 5, and 10 MPa compared to the sample deformed at an effective pressure of 30 MPa. This distinction is further highlighted in the curves of porosity against axial strain, shown in Fig. 2b. Notably, we observe dilatant behaviour in the samples deformed at an effective pressure of 10 MPa and lower, whereas the 30 MPa sample compacted monotonously throughout the experiment. Figure 2c shows an example of the first type of failure mode (brittle/dilatant), showing differential stress and cumulative acoustic emission energy as a function of axial strain (both curves are independent proxies for damage in the sample). In each of the dilatant experiments (i.e. $P_{eff}$=0, 5, or 10 MPa), an initially convex slope can be observed in the stress-strain curves, typical of the closure of pre-existing microcracks aligned approximately perpendicular to the direction of loading. As can be observed in Fig. 2b, this corresponds to an initial decrease in porosity with the initial closure of
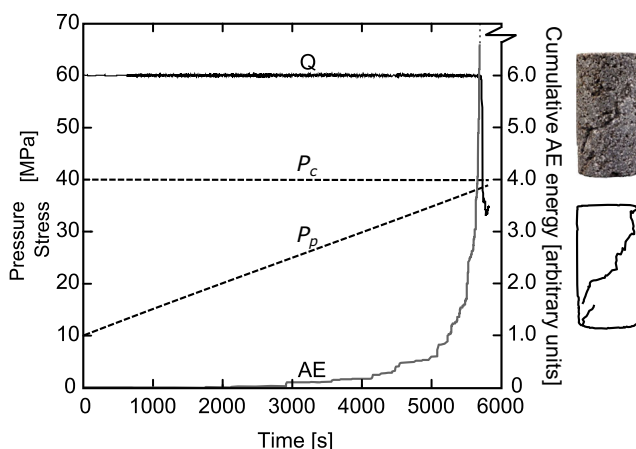
microcracks. $C'$ (shown in Fig. 2c) defines the onset of dilatant microcracking (Wong et al. 1997), after which point the rate of compaction decreases. Samples subsequently underwent axial splitting ($P_{eff}$=0 MPa), or shear fracturing ($P_{eff}$=5, 10 MPa), following peak stresses ($\sigma_P$) of 35.7, 73.5, and 91.1 MPa, respectively (Table 1). The rate of acoustic emissions accelerates significantly prior to sample failure, indicating an increase in the rate of microcracking events as brittle failure is approached (Fig. 2c).

When deformed at an effective pressure of 30 MPa, a different failure mode is observed. The sample responds in a purely compactant manner, associated with monotonously decreasing porosity with increasing strain (Fig. 2b), and the capacity of the material to deform to a substantial strain without failing (Fig. 2d). We refer to this mode of failure as compactant. The onset of inelastic deformation (shear-enhanced compaction) is termed $C^*$ (Wong et al. 1997;

Wong and Baud 2012) and is indicated on Fig. 2d. After $C*$ (which occurred at a differential stress of about 103 MPa in the experiment of Fig. 2d), the differential stress plateaus at around 120 MPa, punctuated by small stress drops. During compactant deformation, we do not observe a distinct acceleration in the AE rate, rather—and as shown in Fig. 2d—there is a relatively steady and progressive accumulation of damage throughout the experiment. Notably, the cumulative AE energy is over an order of magnitude higher than that recorded in the brittle tests (e.g. Fig. 2c) indicating that significantly more damage has been accumulated by the sample, in agreement with previous studies on porous rocks (Wong et al. 1997).

## Increasing pore pressure under constant differential stress

During periods of volcanic unrest and magma ascent in an open system, intact rock in the edifice will likely be subjected to positive excursions in pore pressure (e.g. Heiken et al. 1988; Day 1996). The second suite of tests therefore explores the effect of increasing pore pressure whilst maintaining a constant differential stress and confining pressure (comparable to the lithostatic pressure) on the sample (see Fig. 3 for an example). In each of these tests, despite the order of magnitude differences in pore pressure increase rate (pore pressure was increased at servo-controlled rates of $5.0 \times 10^{-1}$, $5.0 \times 10^{-2}$, $5.0 \times 10^{-3}$, or $5.0 \times 10^{-4}$ MPa s$^{-1}$), increasing pore pressure ultimately culminated in shear fracturing. A photograph (and interpretative sketch) of one of the fractured samples is provided in Fig. 3. Notably, these
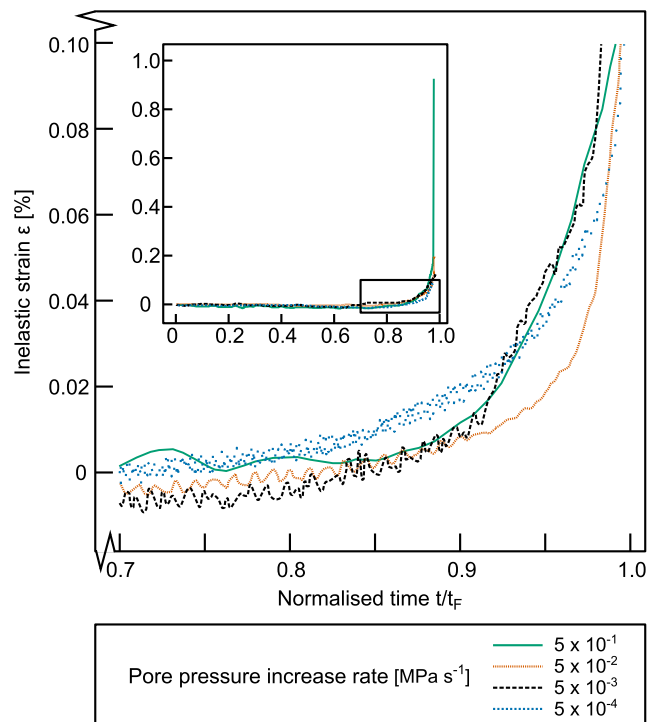
faults are characteristically identical to those resulting from the conventional compressive tests under a constant strain rate (the tests of the preceding section). Brittle failure was achieved on the order of 1, 10, 100, and 1000 min, at effective pressures of 0.4, 1.0, 1.3, and 4.9 MPa, according to the pore pressure increase rates of $5.0 \times 10^{-1}$, $5.0 \times 10^{-2}$, $5.0 \times 10^{-3}$, and $5.0 \times 10^{-4}$ MPa s$^{-1}$, respectively (Table 1). In each case, failure (defined by the large stress drop) was precursed by an acceleration of the AE energy rate, an example of which is provided in Fig. 3, and is comparable—both in terms of shape and magnitude—to the AE activity observed during the brittle constant strain rate tests (Fig. 2c). Despite the large variation (4 orders of magnitude) in pore pressure increase rate, when the time is normalised to the time-to-failure, as in Fig. 4, we see that the acceleration behaviour in strain observed prior to failure is essentially the same.

## Pore pressure oscillation under constant differential stress

Positive pore pressure excursions within a volcanic system may not always culminate in the generation of macroscopic fractures but can increase the level of damage within the edifice. To assess this concept, a further test was performed where a sample was held under a constant confining pressure and differential stress and the pore pressure was oscillated at regular intervals. Starting with confining and pore pressures of 40



Fig. 3 Example of a sample under a constant differential stress where pore pressure was increased monotonously until failure. Time represents the time elapsed since the initiation of pore pressure increase. Pore pressure is increased (in this case, at a rate of $5.0 \times 10^{-3}$ MPa s$^{-1}$) from 10 towards 40 MPa (the confining pressure, maintained constant throughout). Failure is manifested by the drop in differential stress, and a rapid acceleration in cumulative AE. The sample (post-failure) is shown, along with an interpretive sketch of the fault. $P_p$ = pore pressure, $P_c$ = confining pressure, $P_{eff}$ = effective pressure, and $Q$ = differential stress



Fig. 4 Inelastic strain as a function of normalised time (time as a proportion of time-to-failure) for four samples where pore pressure was increased at the set rates ($5 \times 10^{-1}$, $5 \times 10^{-2}$, $5 \times 10^{-3}$, $5 \times 10^{-4}$ MPa s$^{-1}$). The main figure shows the accelerating portion of the strain-time curve. The full curves are shown in the *inset*

and 10 MPa, respectively, pore pressure was increased at a rate of $5.0 \times 10^{-2}$ MPa s$^{-1}$ until 20 MPa, then decreased back to 10 MPa at the same rate. This process was iterated three times, whilst AE was monitored, before increasing the pore pressure to 25 MPa and repeating the process. Finally, pore pressure was increased to 30 MPa, after which the sample failed via a shear fracture. Figure 5 shows the imposed pore pressures for this test, and the accompanying acoustic emission data, given here as the AE rate. We observe that peaks in pore pressure are associated with increases in the rate of acoustic emissions. In detail, we notice that large increases in the rate of AE activity correspond to the point at which the pore pressure is increased to a value higher than that previously applied to the rock (marked by the arrows on Fig. 5). In contrast to the experiments of the previous section where pore pressure was achieved at relatively low effective pressures (<5 MPa), this sample failed at an effective pressure of approximately 12.4 MPa.

## Pore pressure increase during constant strain rate deformation

Whereas the experiments in the two preceding sections are analogous to the impact of the infiltration of pore fluids into otherwise intact rock at a constant stress, this section addresses positive pore fluid excursions in concert with ongoing compactive deformation. This scenario was imposed on a sample by deforming at an effective pressure of 30 MPa ($P_c = 40$ MPa and $P_p = 10$ MPa) and a strain rate of $10^{-5}$ s$^{-1}$, conditions that were maintained until the sample reached 3.5 % axial strain. At this strain, and during the deformation of the sample, pore pressure was increased at a rate of $5.0 \times 10^{-2}$ MPa s$^{-1}$ to 35 MPa (i.e. $P_{eff} = 5$ MPa). Deformation was arrested at an axial strain of 5 %. The goal here was to instigate brittle deformation in a sample deforming in the compactant regime. The mechanical data for this experiment indicate that, after $C*$, the sample underwent shear-enhanced compaction, and deformation followed a similar path to the compactant experiment shown in Fig. 2d. During

this period, porosity decreased consistently with increased axial strain (monitored using the pore pressure intensifier). The imposed increase in pore pressure propagated a dilatant shear fracture, accompanied by a significant stress drop (to a level comparable to the post-failure residual stress $\sigma_F$ of Fig. 2b: $P_{eff} = 5$ MPa). Beyond 3.5 % axial strain, the there is a brief period where the induced volumetric strain is negligible. However, very quickly following the initiation of pore pressure increase, the compactant behaviour occurring due to the constant strain rate deformation is overcome by the dilatant behaviour induced by the increasing pore fluid pressure. Once the pore pressure had reached 35 MPa, it was maintained at this level, during which time the sample continued to dilate. The response of the confining pressure pump affirms that by the end of the experiment, the sample had gained volume (i.e. porosity) relative to its initial condition. Thus, the sample underwent both compactant and dilatant (brittle) deformation, manifest by barrelling of the sample overprinted by a shear fracture (as shown in the photograph and interpretative sketch in Fig. 6).

## Discussion

### Operative micromechanical processes

Previous work (e.g. Kennedy et al. 2009; Zhu et al. 2011; Loaiza et al. 2012; Adelinet et al. 2013; Heap et al. 2015a, c) has shown that triaxial deformation of porous volcanic rocks can culminate in one of two failure modes—dilatant (macroscopically brittle) or compactant—both of which are governed by different dominant microstructural processes. Brittle failure arises due to the formation and growth of dilatant microcracks which coalesce into a macroscopic fracture through the sample, either as an axial split (in the case of unconfined rock) or a shear fracture (under confining pressure). Failure in this manner can be seen in Fig. 3 (inset); the acceleration in AE
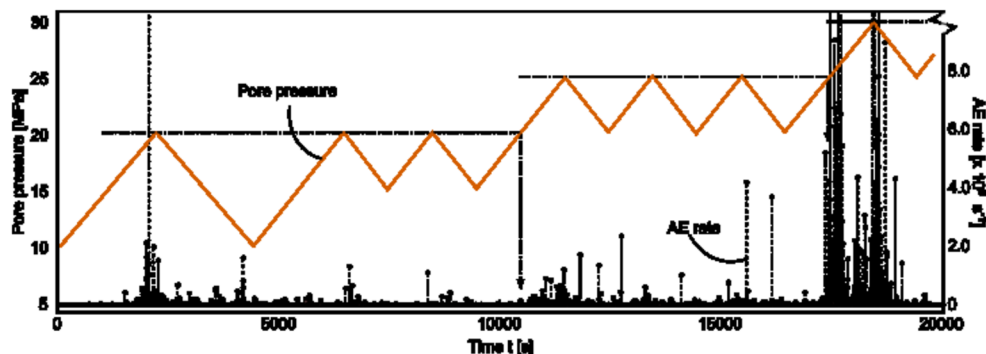


**Fig. 5** Pore pressure and AE rate for a sample where pore pressure was oscillated throughout the test. Peaks in the pore pressure cycling are associated with rapid increases in the AE rate. Brittle failure occurs as the pore pressure is increased from 25 to 30 MPa. *Dashed lines* and *arrows* indicate where surges in AE rate are observed when pore pressure is increased to a previously unseen level. Refer to text for discussion
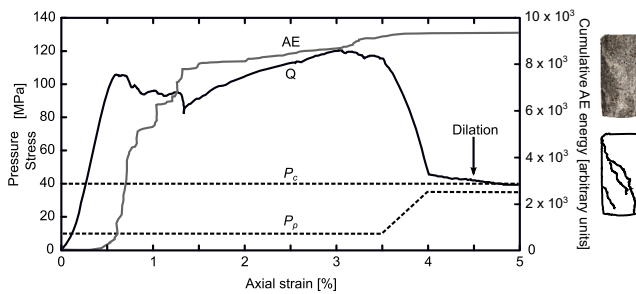
**Fig. 6** Pore pressure increase under constant strain rate deformation. The stress-strain curve shows that the sample failed in a compactive manner (as in Fig. 2a, d). The strain rate of $10^{-5}$ s$^{-1}$ was maintained, and after the sample had been subject to 3.5 % axial strain, the pore pressure was increased from 10 to 35 MPa. The photograph shows the sample post-failure, with an interpretive sketch illustrating the fault. The sample has undergone both barrelling (compaction) and shear fracture (dilation). AE is also shown: whilst the pore pressure is maintained at 35 MPa, there is a negligible amount of AE accumulated

in this figure is also indicative of the process of dilational microcracking. Contrastingly, compactant deformation of volcanic rocks has been shown to be governed by cataclastic pore collapse which can be either diffuse (e.g. Zhu et al. 2011; Heap et al. 2015c) or localised (e.g. Loaiza et al. 2012; Adelinet et al. 2013; Heap et al. 2015a). Compaction localisation in andesite is thought to be associated with small drops in axial stress (Heap et al. 2015a); given that the same rock type was used in this study and that of Heap et al. (2015a), we anticipate that the stress drops discernible in Fig. 2d are coincident with the formation of bands of collapsed pores.

### Stress paths and failure modes of edifice-forming andesite

Compiled data from this study and that of Heap et al. (2015a) have been plotted in order to map the failure envelope for andesites from Volcán de Colima, on axes of differential stress $Q$ and effective mean stress $P$, determined by $P = (\sigma_1 + 2\sigma_3)/3 - P_p$ (where $\sigma_1$ is axial pressure, and $\sigma_3$ is the confining pressure). The failure envelope, shown in Fig. 7a, is defined in the brittle field by differential stress at failure, i.e. the peak stress ($\sigma_P$); in the compactive field, failure (yield) is defined at the threshold $C^*$, the onset of shear-enhanced compaction (Table 1). A further margin can be delineated by differential stress at $C'$, the onset of dilant microcracking. The failure envelope therefore defines the conditions in $P$-$Q$ stress space whereat these andesites are inelastically deformed or otherwise (Wong et al. 1997), for a strain rate of $10^{-5}$ s$^{-1}$. At stresses outside the failure envelope, the rock will have undergone mechanical failure. Between the brittle envelope and that defined by the onset of microcracking, samples are damaged but have not undergone macroscopic failure. Finally, the portion of the graph described by the damage envelope and the

compactive failure envelope are conditions under which the rocks are intact, whereby any deformation imposed on the sample is nominally elastic (recoverable).

The brittle envelope shows that differential stress at failure is a linear function of the effective mean stress, in agreement with the Mohr-Coulomb failure criterion. A previous study on the failure modes of porous andesite (Heap et al. 2015a) suggests that the yield cap is similarly close to linear in the compactant regime, due to the combination of microcracks and pores comprising the total porosity (Heap et al. 2015a; also discussed in Zhu et al. 2010 for limestones containing micro- and macroporosity). This is contrast to typical yield caps for porous sandstones, for example, which tend to be elliptical (e.g. Wong and Baud 2012).

Figure 7b–d shows the stress paths of samples for the three types of experiment in which the pore pressure was increased until brittle failure, as described previously (i.e. the tests of Figs. 3, 5, and 6). The trajectory of each stress path is simply the differential stress and calculated effective mean stress for each timestep during the corresponding experiments. In each case, the initial stress path (shown by the dotted line) begins at a differential stress of zero ($Q = 0$) and an effective mean stress determined by the initial pore and confining pressures imposed on the sample. In Fig. 7b, the path moves from this point to a differential stress of 60 MPa and an effective mean stress of 50 MPa as the samples are deformed triaxially. The differential stress is then maintained constant as pore pressure is increased as described previously. In these cases, the stress path (solid line) moves horizontally from an intact condition towards the $y$-axis, until failure (Fig. 7b). We observe that, irrespective of the pore pressure increase rate ($5.0 \times 10^{-1}$ to $5.0 \times 10^{-4}$ MPa s$^{-1}$), the samples fail at (or very close to) the brittle failure envelope. This is in agreement with the inelastic strain rate data (Fig. 4), from which we can infer that, at least on timescales from approximately 1 min to 1 day, the process of embrittlement appears essentially rate-independent. At this scale, any influence of time-dependent processes such as stress corrosion cracking (physicochemical deformation: see Brantut et al. 2013 for a review) cannot be decoupled from the natural variability of our samples.

In Fig. 7c, the initial stress path is identical to that in Fig. 7b. However, in this case, the pore pressure is cycled until sample failure (as shown in Fig. 5). Again, we observe that the stress path moves horizontally towards the $y$-axis, but sample failure is initiated beneath the brittle envelope. The corresponding cumulative acoustic emission data—a proxy for the amount of damage accumulated by the sample—for the constant differential stress experiments shown in Fig. 7b, c are comparable. This remarkable similarity (shown in Fig. 8) indicates that failure will occur when a threshold amount of damage has accumulated, regardless of the rate of pressure increase. This is a similar observation to those made during experiments designed to investigate the time dependency of
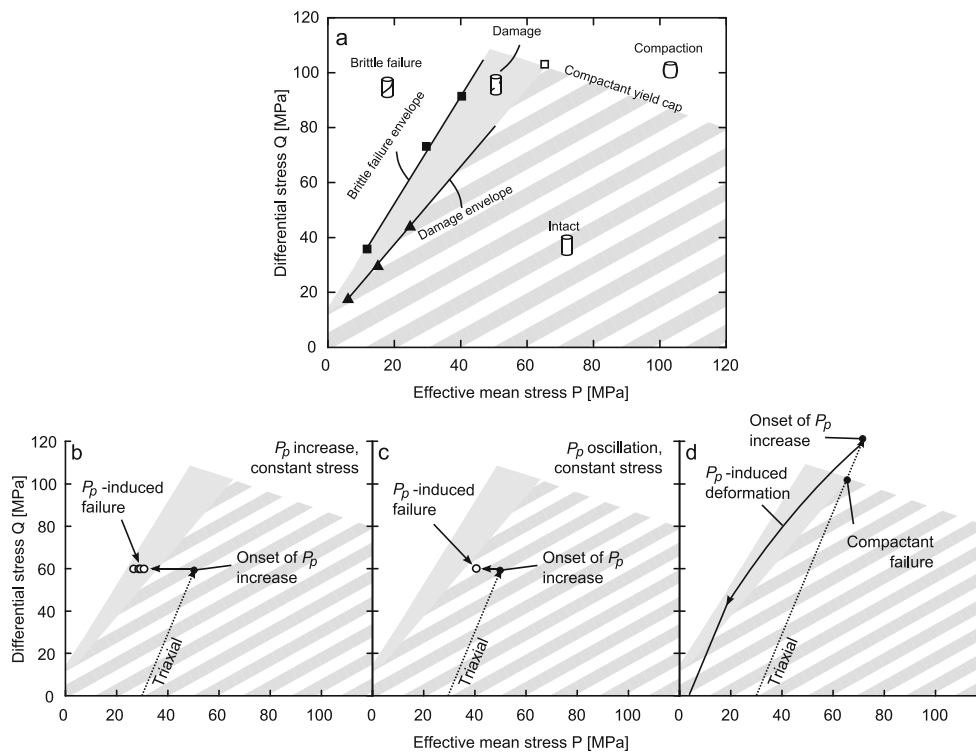
**Fig. 7** **a** Compiled experimental data from this study in the stress space (differential stress $Q$ as a function of effective mean stress $P$). *Closed symbols* indicate brittle experiments ($P_{eff}$ of 10 or lower), and *open symbols* show compactant experiments. The mode of failure we would observe in each regime of the diagram is illustrated by the cartoons: cracking and brittle failure, compaction, and intact rock. The slopes of the brittle failure and damage envelopes are described by $Q = 1.9614P + 13.207$ and $Q = 1.3992P + 9.4652$, respectively. **b**–**d** Pore pressure-embrittled samples in the context of this envelope (symbols are omitted for clarity). In each case, the *dotted line* represents the initial triaxial loading of the sample, to the point in the experiment when the pore pressure was increased. The subsequent stress path is shown by the *solid line*. In **b**, samples were brought to failure by increasing the pore pressure monotonously at different rates ($5 \times 10^{-1}$, $5 \times 10^{-2}$, $5 \times 10^{-3}$, and $5 \times 10^{-4}$ MPa s$^{-1}$), under constant differential stress. In these cases, all the samples fail on or near to the brittle failure envelope. In **c**, the iterative increase of the pore pressure resulted in sample failure well within the failure envelope. Finally, in **d**, the sample was deformed triaxially at an effective pressure of 30 MPa until it failed in the compactant regime (the point where it crosses the compactant yield cap). The stress path from the onset of pore pressure increase indicates that the sample transited into the brittle regime, generating a shear fault at some (unknown) point on this path

rock deformation (e.g. Kranz and Scholz 1977; Baud and Meredith 1997), whereby the final stage of deformation occurs when a critical threshold in event number or energy is surpassed, independent of the stress on the sample (we observe failure in these porous andesites when the cumulative energy under the recorded waveform—in the arbitrary units defined previously—is between $2 \times 10^1$ and $2 \times 10^2$).

Finally, Fig. 7d shows the stress path of the experiment shown in Fig. 6, in which the pore pressure was increased during constant strain rate deformation, as described in the preceding section. The sample deforms poroelastically before passing $C^*$ (i.e. the onset of shear-enhanced compaction) during constant strain rate triaxial deformation. Since the sample is deformed to a differential stress higher than $C^*$, the sample reaches a stress-state above the compactive yield envelope. Following the onset of pore pressure increase, the stress condition of the sample changes such that it moves along a path towards the brittle envelope (as shown in Fig. 7d); a shear

fracture develops as the sample moves along this path (as shown in the photograph of Fig. 6).

## Volcanic edifice embrittlement

### Outgassing and eruptive behaviour

Our experiments show that pore pressure increase can cause otherwise intact rock—or rock deforming in a compactant manner—to fail through brittle faulting. The mode of failure of porous edifice-forming rocks is of importance due to the consequent effect on edifice permeability. Work by Heap et al. (2015a) shows that a throughgoing tensile fracture in porous andesite can increase permeability, whereas compactant deformation can result in reduced permeability. In an open system, pore pressure increases could therefore result in an increase of edifice permeability, due to the embrittlement induced by
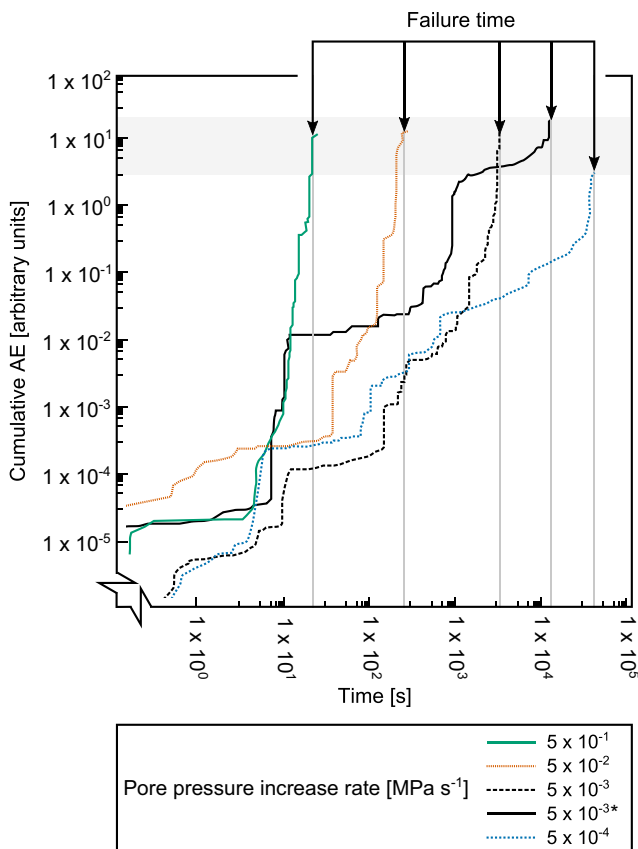
**Fig. 8** Cumulative acoustic energy (cumulative energy under the received waveform, given in arbitrary units) against time, showing the five samples which were brought to failure from an intact stress condition via pore pressure increase: four at different monotonous rates ($5 \times 10^{-1}$, $5 \times 10^{-2}$, $5 \times 10^{-3}$, $5 \times 10^{-4}$ MPa s$^{-1}$), and one by oscillating the pore pressure at $5 \times 10^{-2}$ MPa s$^{-1}$ (marked by an *asterisk*). *Arrows* indicate the failure time of each sample. Notably, all samples fail once a given threshold of damage has been accumulated, represented in our experiments by ~150 arbitrary units of AE energy

these positive excursions. Improved open system outgassing associated with increasing permeability can preclude the buildup of pressure in a volcano, fostering effusive—rather than explosive—activity (e.g. Woods and Koyaguchi 1994; Jaupart 1998). Hence, the propensity for fracture generation within the edifice may well be a critical parameter in limiting explosivity and bridling volcanic hazard at a given site.

Figure 9 illustrates potential outgassing mechanisms arising through pore fluid-induced embrittlement. Note that the colour scale is illustrative and arbitrary: any deviation from equilibrium pore pressure—and indeed the equilibrium pressure—rests on several parameters (porosity, temperature, stress regime, and so on) which are poorly constrained within the edifice. Modelling the absolute magnitudes of pore pressure deviations around the conduit is not the focus of this contribution, other than in a qualitative sense. In the first scenario (Fig. 9a–c), pore pressure in the edifice host rock is increased due to an ascending point source of thermal or mechanical stress, for

example, by a migrating magma batch or gas slug (Fig. 9a) or a magmatic intrusion (Fig. 9b). Close to a conduit or dyke, where we anticipate thermal and mechanical stresses to be highest, we expect the greatest rates and magnitudes of pore pressure increase (as represented in Fig. 9a–c). As a result, and as inferred from our experiments, rock embrittlement (brittle failure) is likely to create a fracture network proximal to the conduit. In our scenario, in the wake of the ascending body, the process of pore fluid-induced embrittlement would therefore leave a fractured zone or halo surrounding the conduit (Fig. 9a–c). If sufficient fractures are generated to constitute a pathway for volatiles, then outgassing can occur (as in Fig. 9c, d), thus mitigating the buildup of pressure beneath a viscous plug or dome, and enhancing lateral outgassing as shown in Figs. 1 and 9e. Indeed, annular outgassing is also predicted for Mono Craters, USA (Rust et al. 2004), Mount St. Helens, USA (Gaunt et al. 2014), and observed at Santiaguito Volcano, Guatemala (e.g. Lavallée et al. 2013). We propose that the appearance of new fumaroles during unrest (or renewed outgassing at closed or sealed fumaroles), as we infer from our thermal emission data (Fig. 1), may be explained by this fracture wake process.

We anticipate that much of the edifice at greater depths will be undergoing inelastic compaction due to the increased lithostatic pressure of accumulating eruptive products (see Heap et al. 2015a). Compactant deformation may also result from stress perturbations associated with periods of volcanic activity (e.g. Gerst and Savage 2004; Roman et al. 2004). Significantly, fracture generation in the deep edifice, as a consequence of pore pressure embrittlement, could offset the decrease in permeability associated with deformation in a compactant regime (Heap et al. 2015a). Thus, transient or sustained pore pressure increases at depth can in fact bring about mechanical behaviour typically expected in the shallower parts of the edifice, effectively transiting the rock from a compactant to a dilatant regime. Shear fault formation in a sample which has already experienced a degree of inelastic compaction (as in our experiment in Fig. 6) illustrates that pore fluid-induced embrittlement can encompass all regions in the edifice, even where the lithostatic pressure would otherwise preclude brittle behaviour. Indeed, fluid-induced embrittlement has been posited at even greater depths (of the order of tens of kilometres beneath the surface) in deep magmatic systems (e.g. Power et al. 2004; Sisson and Power 2013) and subduction environments (e.g. Shiina et al. 2013).

As sketched in Fig. 9f, the formation of deep pore pressure-induced fractures may serve to forge pathways for exsolved volatiles by connecting the near-conduit fracture network with regional fault systems. Thus, this deep-edifice embrittlement mechanism could explain anomalous magmatic gas measurements (for example, as observed at Volcán de Colima: Taran et al. 2000; Varley and Taran 2003) and the ubiquity of LP

**Fig. 9** **a** Cartoon of a plugged volcanic system. Note that the colour scale is for illustrative purposes only: these do not correspond to any measured or modelled values. At a given depth, volatiles will exsolve into a discrete gas phase. From **a** to **b**, the gas phase aggregates and ascends, increasing pore fluid pressure within the edifice due to thermal and mechanical stresses. In **b**, pore pressure-induced fractures initiate in the shallow edifice, creating a fracture network in the wake of the gas slug (equivalently, the ascent of a magmatic body could influence pore fluid pressures in the same manner). Propagation and coalescence of these fractures connect pathways for gases, allowing outgassing around the dome **c**. **d** A cross-sectional schematic of the uppermost region of the edifice and dome, illustrating how iterative pore pressure-induced embrittlement could create a pervasively fractured halo around the conduit, comprising many pathways for gas escape. **e** Shows outgassing through the permeable dome structure at Volcán de Colima, taken in July 2014 (photo credit: Josh Greenwood). Also discernible is outgassing at discrete points in the edifice proximal to the dome. **f** Pore pressure-induced embrittlement in the deeper edifice could permit outgassing, by creating—albeit transiently—pathways from near the volcano and regional fault structures
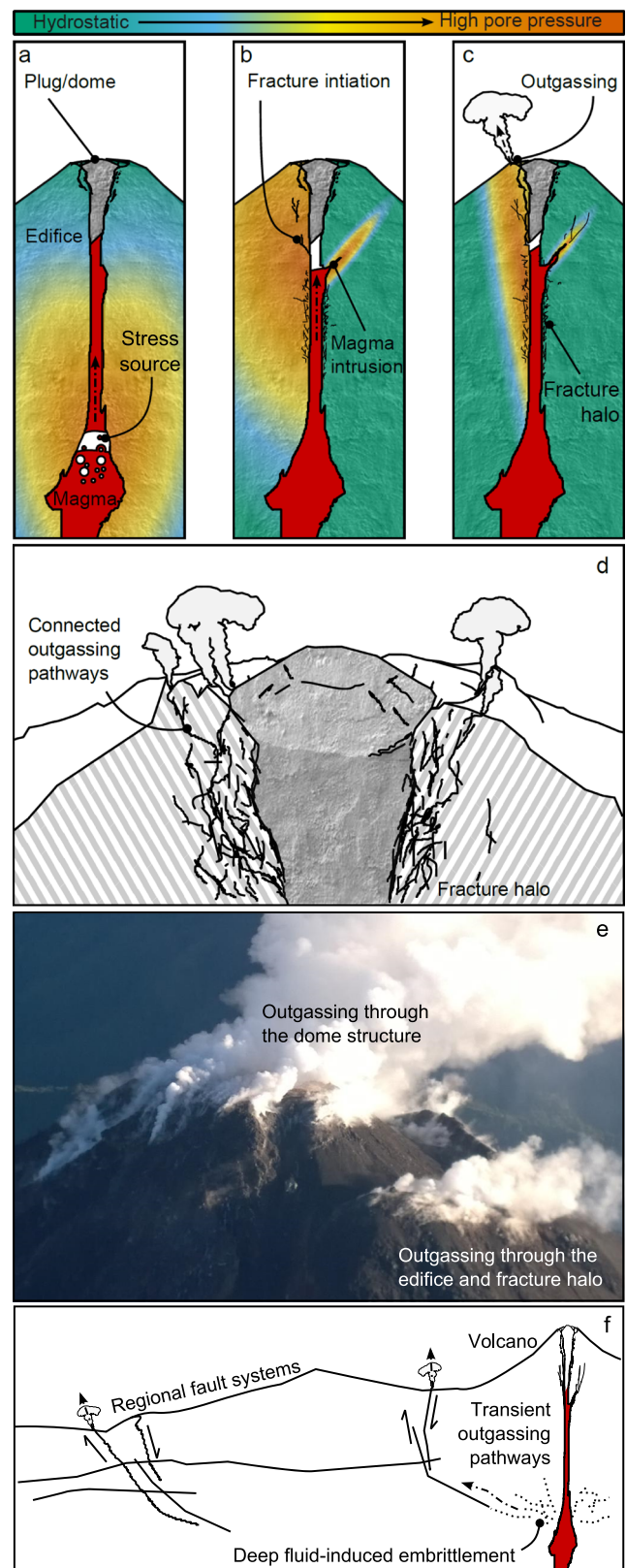


seismic events recorded at many active volcanoes (e.g. Varley et al. 2010; Jousset et al. 2013; Boué et al. 2015). Outgassing of magmatic volatiles through larger-scale regional fault systems is also supported by field studies of other volcanic systems (e.g. Heiligmann et al. 1997; Giammanco et al. 1998). An increase in edifice permeability through deep fracturing is however likely transient, resting on the initial permeability and porosity of the system, duration and magnitude of pore pressure deviation, and the capacity for fractures to close or heal. Fracture closure can occur simply due to the overlying lithostatic pressure (e.g. Nara et al. 2011), and fracture healing could occur as a result of hydrothermal mineral precipitation (e.g. Edmonds et al. 2003) or the hot isostatic pressing of fragmented material within fractures (e.g. Kolzenburg et al. 2012).

## Edifice stability and seismicity

Pore pressure fluctuations can directly increase the density of fractures within the edifice, resulting in a subsequent decrease in edifice integrity, particularly if fractures are propagated at or proximal to a structurally critical point (Elsworth et al. 1996; Lagmay et al. 2000; Thomas et al. 2004; Gudmundsson 2011). In the case where even relatively small overpressures can develop (e.g. when the pore pressure is 0.5 MPa greater than the confining/lithostatic pressure), rock strength has been shown numerically to be reduced by about an order of magnitude (Heap et al. 2015b). Further, decompression events, compromising flank or dome stability (e.g. Collinson and Neuberg 2012), may be triggered if pore pressure-induced fractures can access overpressurised magma. Indeed, it has been shown experimentally (Lavallée et al. 2011; Benson et al. 2012) that magma fragmentation can be a direct consequence of wall rock failure. In turn, this suggests that positive pore pressure excursions and host rock embrittlement close to

the conduit could also bring about decompression and magma fracture. Reduction of structural integrity can give rise to an

array of hazards, ranging from relatively harmless rockfalls (e.g. Mueller et al. 2013) to partial flank collapse and the instigation of pyroclastic density currents (Day 1996; Reid et al. 2000; Watters et al. 2000).

During the pore pressure oscillation experiment, we notice that each increase in pore pressure to a previously unseen level is coincident with a surge in AE rate (Fig. 5). This is in agreement with the Kaiser "stress-memory" phenomenon, whereby damage (i.e. new microcracking) only occurs once a threshold level of stress—equivalent to the previous maximum stress imposed on the material—is exceeded (Kaiser 1953; see also Lavrov 2003 for a review). This effect has been observed in cyclic stressing experiments on volcanic rock (Heap et al. 2009; Kendrick et al. 2013). Moreover, a recent study (Heimisson et al. 2015) proves—through the analysis of contemporaneous geodetic and seismic data—the occurrence of the Kaiser effect at the kilometre scale within the Krafla caldera, Iceland. In our experiments, the observation of this phenomenon indicates that there is also a complex stress-memory effect associated with repeated oscillations in pore fluid pressure in the edifice. Eventually, iterative damage of the edifice rock by pore pressure excursions may result in brittle failure due to the cumulative effect of discrete microcracking events over time (as in Figs. 5 and 8). Whether subject to a constant pore pressure increase or iterative transient increases, our data indicate that, for a given porosity, failure and embrittlement of edifice rocks will occur after a threshold amount of damage is accumulated, irrespective of the pore pressure increase rate. This suggests that if the rock has previously accumulated a large amount of damage (i.e. close to the threshold amount), then only a relatively small increase in pore pressure would be necessary to trigger failure.

Further, it is reasonable to assume that pore fluid-induced embrittlement will contribute to the seismic record as suggested by Nishi et al. (1996), evidenced by the AE activity associated with sample damage in our experiments (Figs. 2, 3, 5, and 8). Recent studies (Palo et al. 2009; Petrosino et al. 2011) identify LP events both in the shallow edifice of Volcán de Colima (i.e. 1 km depth or less) and in deeper edifice regions (up to 4 km) and suggest that these typically arise from a non-repeating source. Whilst this style of seismic activity is often observed to coincide with explosive activity (e.g. Hagerty et al. 2000; Arciniega-Ceballos et al. 2003), this is not always the case (e.g. Kumagai et al. 2002; Petersen et al. 2006). Whether long-period seismicity at volcanoes is a result of shear fracturing (e.g. Neuberg et al. 2006; Varley et al. 2010; Thomas and Neuberg 2012), slow-rupture failure of volcanic materials (e.g. Harrington and Brodsky 2007; Bean et al. 2014), or the resonance of fluid-filled cracks (e.g. Lahr et al. 1994; Neuberg 2000; Benson et al. 2008; De Lauro et al. 2012), we note that these interpreted mechanisms are all generally congruent with embrittlement as outlined in this study: a seismogenic process which is anticipated to occur throughout the edifice. We note that the coupling of fluid migration and brittle fracturing processes could yield complex seismic signals comprising both short- and long-period frequency elements.

## Conclusion

The effective pressure imposed on a rock, a factor important in dictating its mechanical response and failure mode, can be decreased by an increase in the pore pressure. This process is anticipated throughout volcanic edifices, especially in the thermally and mechanically stressed region proximal to the conduit. Through a suite of triaxial experiments on andesitic rocks—designed to explore the influence of pore pressure excursions on the failure mode of the rocks within a volcanic edifice—we show that brittle failure (fracturing) can be induced in an otherwise intact rock by simply increasing the pore pressure. Increasing the pore pressure at different rates, ranging from $5 \times 10^{-1}$ to $5 \times 10^{-4}$ MPa s$^{-1}$ yields comparable AE and strain acceleration behaviour relative to time-to-failure, and samples fail at equivalent effective pressures. Over the timescales of our experiments—on the order of 1 min to 1 day—conclusive evidence for time-dependent processes (such as stress corrosion) was not seen. Cumulative damage due to pore pressure oscillation can cause failure under stress conditions well below the short-term strength of the rock, with failure the result of accumulating a threshold amount of damage. As a result, failure occurs at a relatively higher effective pressure in this case. We further show that pore pressure-induced embrittlement can occur in rock deforming in the compactant regime, indicating that fracture generation can occur in regions of the edifice where brittle deformation would be precluded otherwise. Thus, pore fluid-induced embrittlement is likely to occur not only in shallow (low confining pressure) regions of the edifice under a constant differential stress but also in regions that are deeper or closer to the conduit, where the rock is liable to be deforming in a compactant manner. Magma fragmentation, fluid migration, flank destabilisation, and associated seismicity are all potential effects of this process. Nonetheless, by increasing the fracture network throughout the edifice, particularly in the rock surrounding the conduit, pore pressure excursions may serve to locally increase permeability and in turn improve lateral outgassing within volcanic systems, promoting effusive—rather than explosive—activity.

## Appendix A: Effective pressure law for andesite

Any loading of a saturated porous medium is defined by the stress components $\sigma_{ij}$ and the pore fluid pressure $P_p$. Moreover, if the poromechanical response of said medium to an applied stress coincides with that of the stress difference $\sigma_{ij} - \alpha P_p \delta_{ij}$, then the latter quantity is referred to as the effective stress $\sigma_{ij}$. In particular, if the coefficient $\alpha$ is unity, then the quantity $\sigma_{ij} - P_p \delta_{ij}$ corresponds to Terzaghi's formulation, often called "Terzaghi's effective stress" or "Terzaghi's principle" (Terzaghi 1923; Baud et al. 2015). For elastic deformation, the effective stress law can be derived from the linear theory of poroelasticity (Berryman 1992; Wang 2000) with the effective stress coefficient given by the Biot-Willis coefficient $\alpha$, whereby $0 \leq \alpha \leq 1$ (Biot 1941; Paterson and Wong 2005). For inelastic deformation and failure, $\alpha$ can be determined experimentally.

In conventional triaxial deformation experiments, this simple effective stress law is defined in terms of an effective pressure, whereby $P_{eff} = P_c - \alpha P_p$; $P_{eff}$ and $P_c$ being the effective and confining pressures, respectively. Simply put, in the case where $\alpha = 1$, the stress regime on a sample deformed at respective confining and pore pressures of 10 and 15 MPa would be identical to that imposed with confining and pore pressures of 100 and 105 MPa, respectively (the effective pressure would be 5 MPa in both cases). In contrast, if the volumetric response of the fluid and solid constituents are unequal and $\alpha < 1$, then the stress regimes in the two scenarios will differ. In essence, this means that the measured failure stress of a sample would be different in each scenario, all other parameters being equal. There exists a paucity of data on this coefficient for the failure of porous rocks, largely due to the natural variability between samples, which makes its determination often challenging and sometimes quite impossible.

Since we present triaxial experiments at different pressures in this study, it is important to verify that the effective pressure coefficient does not differ significantly from unity in porous andesites. We therefore performed a series of constant strain rate triaxial tests at the same nominal effective pressure according to Terzaghi's principle (i.e. $P_{eff}$ if $\alpha = 1$), but imposing different confining and pore pressures. In an attempt to minimise sample variability, we selected samples that contained the same connected porosity. The experimental conditions and differential stress at failure are given in Table 2.

Herein, we calculate $\alpha$ as the value that equalises the ratio of minimum and maximum peak stresses ($\sigma_{Pa}$ and $\sigma_{Pb}$) and the ratio of the corresponding effective pressures ($P_{eff a}$ and $P_{eff b}$):

$$\frac{\sigma_{Pa}}{\sigma_{Pb}} = \frac{P_{eff a}}{P_{eff b}} \approx 0.73 \tag{A1}$$

which occurs when $\alpha \approx 0.98$, a value comparable to that determined recently by Baud et al. (2015) for Bleurswiller sandstone. However, we note that the natural variability in strength of these andesites is high: samples A5-09 and A5-11 were deformed under identical experimental conditions, yet there is a discrepancy of 18.68 MPa between their differential stresses at failure. Given the level of natural heterogeneity in these andesites (a result of their complex and variable microstructure)—and indeed, in other intrusive and extrusive igneous rocks—we highlight that our data are not sufficient to state conclusively that the effective pressure coefficient differs significantly from unity in these materials. Nevertheless, although we cannot constrain the exact value of the Biot-Willis coefficient in these andesites, this pilot study does confirm that the true value is not likely to differ significantly from unity. As such, the use of Terzhagi's principle of effective pressure in our tests is a valid assumption.

## Appendix B: Sample drainage

If the deformation of a sample proceeds at a rate faster than the response time of the pore pressure intensifier/volumometer, the experiment is considered "undrained". In such a scenario,

**Table 2** Porosity, pressure conditions, and differential stress at failure for porous A5 andesite. $P_p$, $P_c$, and $P_{eff}$ correspond respectively to the pore, confining, and effective pressures and are all given in MPa

| Sample | Porosity | $P_p$ | $P_c$ | $P_{eff} = P_c - \alpha P_p$ | | Peak differential stress $\sigma_P$ [MPa] |
|---|---|---|---|---|---|---|
| | | | | $\alpha = 1$ | $\alpha = 0.9794$ | |
| A5-09 | 0.09 | 55 | 60 | 5 | 6.13 | 138.87 |
| A5-11 | 0.09 | 55 | 60 | 5 | 6.13 | 157.55 |
| A5-13 | 0.09 | 105 | 110 | 5 | 7.16 | 177.61 |
| A5-17 | 0.09 | 10 | 15 | 5 | 5.21 | 128.83 |
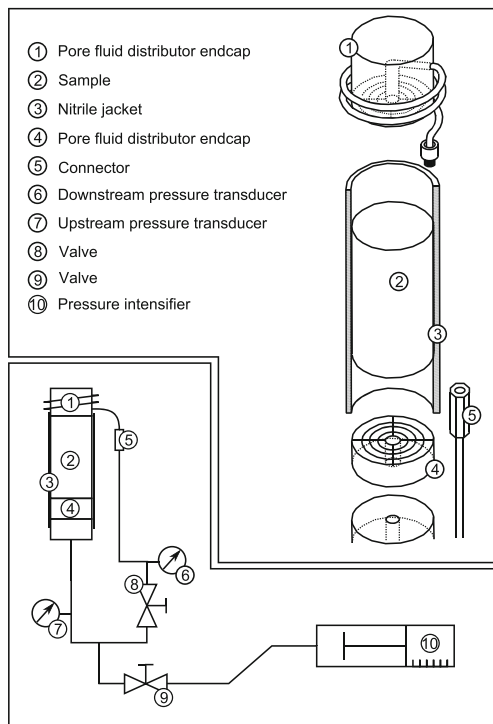
**Fig. 10** Schematic of the setup used to test sample drainage. When the upstream valve is open, pore pressure within the sample can be increased or decreased by the intensifier (10). If the downstream valve is open, then the pore pressure circuit is fully connected. However, when (9) is open and (8) closed, the pressure response measured at (6) depends on whether or not the sample is fully saturated

the tips of fast growing dilatant microcracks would not be fluid-saturated; this not only provides an underestimate of the porosity change during deformation but also influences the mechanical behaviour of the rock. Sample drainage was an important consideration in the experiments presented herein because we are interested in the mechanical response of a rock as pore pressure is increased. If our experiments were undrained, there would be a discrepancy between the pore pressure we expect in the rock, and the pore pressure within the rock. This would further complicate matters by creating a heterogeneous pore pressure distribution within the sample. In order to assess whether our samples were drained (i.e. fully saturated) during all the experiments, the setup shown in Fig. 10 was used. This experimental setup allows the increase or decrease of pore pressure using an intensifier whilst monitoring both up- and downstream pressure. When the downstream valve (8 in Figure 10) is closed, any pressure deviation measured by the downstream transducer (6 in Figure 10) must first have flowed through the sample. By servo-controlling the upstream pore fluid pressure and monitoring the downstream pressure, we can thus determine whether the sample is drained at different pressure increase rates. Pore pressure was oscillated between 10 and 20 MPa, whilst confining pressure was maintained at 40 MPa. Pressure was cycled at incrementally faster rates, from an initial value of $5.0 \times 10^{-2}$ MPa s$^{-1}$, to a final rate of $5.0 \times 10^{-1}$ MPa s$^{-1}$. If the sample were undrained, we
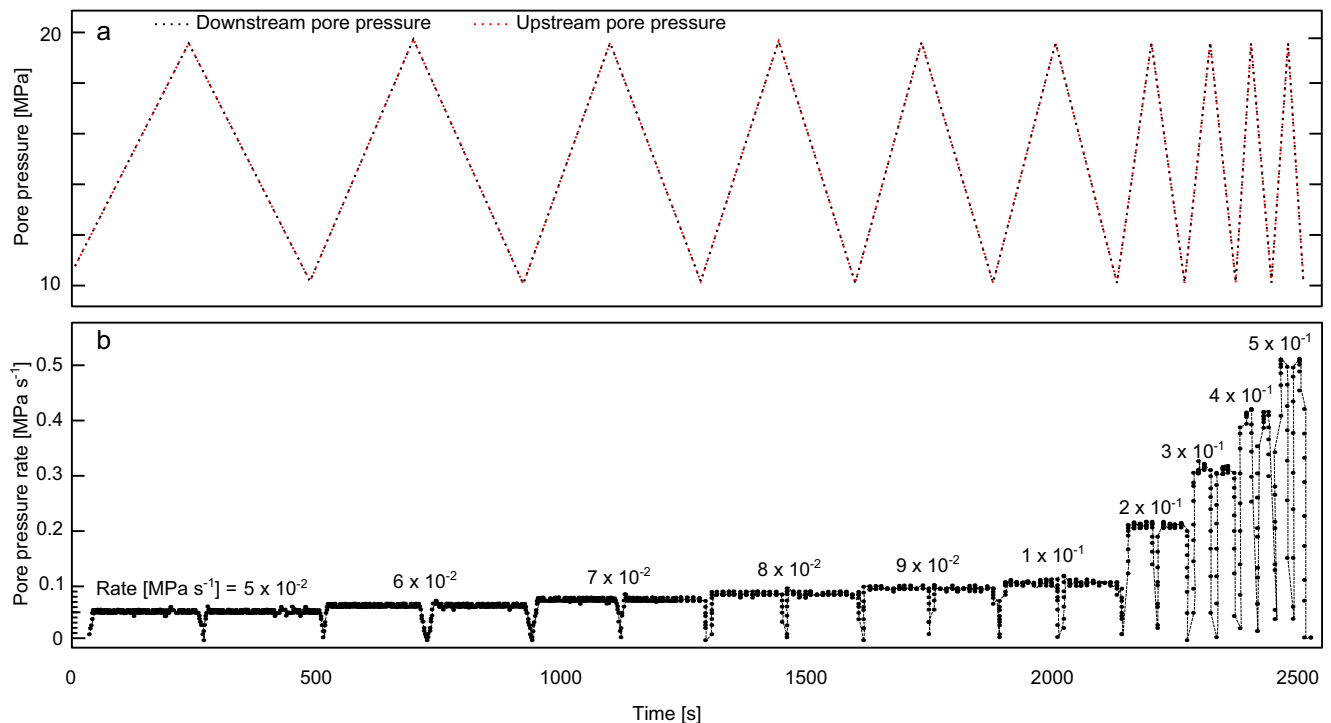


**Fig. 11** Mechanical data from a triaxial experiment designed to examine sample drainage in porous andesitic rock (sample C8). **a** Graph of pore pressure against time showing the monitored upstream (*red dotted curve*) pressure as a function of changing downstream (*black dotted curve*) pressure. **b** Graph of pore pressure rate against time showing the (absolute) rate of pore pressure change during the experiment

would expect to see a delay in the response of the downstream pressure relative to the upstream pressure. However, as shown in Figure 11, no delay can be seen. This indicates that the permeability of these porous andesites is sufficiently high to preclude sample desaturation, even at significantly high rates of pore pressure increase.

# References

Adelinet M, Fortin J, Schubnel A, Guéguen Y (2013) Deformation modes in an Icelandic basalt: from brittle failure to localized deformation bands. J Volcanol Geotherm Res 255:15–25

Anderson KR, Poland MP, Johnson JH, Miklius A (2015) Episodic deflation–inflation events at Kīlauea Volcano and implications for the shallow magma system. Hawaiian Volcanoes: From Source to Surface 208:229

Arciniega-Ceballos A, Chouet BA, Dawson P (2003) Long-period events and tremor at Popocatepetl Volcano (1994–2000) and their broadband characteristics. Bull Volcanol 65:124–135. doi:10.1007/s00445-002-0248-8

Auker MR, Sparks RSJ, Siebert L, Crosweller HS, Ewert J (2013) A statistical analysis of the global historical volcanic fatalities record. J Appl Volcanol 2(1):1–24

Baud P, Meredith PG (1997) Damage accumulation during triaxial creep of Darley Dale sandstone from pore volumometry and acoustic emission. Int J Rock Mech Min Sci 34(3):24–e1

Baud P, Zhu W, T-f W (2000) Failure mode and weakening effect of water on sandstone. J Geophys Res Solid Earth 105(B7):16371–16389. doi:10.1029/2000JB900087

Baud P, Reuschlé T, Ji Y, Cheung CS, Wong TF (2015) Mechanical compaction and strain localization in Bleurswiller sandstone. Solid Earth, Journal of Geophysical Research

Bean CJ, De Barros L, Lokmer I, Métaxian JP, O'Brien G, Murphy S (2014) Long-period seismicity in the shallow volcanic edifice formed from slow-rupture earthquakes. Nat Geosci 7(1):71–75

Benson PM, Heap MJ, Lavallée Y, Flaws A, Hess KU, Selvadurai APS, Dingwell DB, Schillinger B (2012) Laboratory simulations of tensile fracture development in a volcanic conduit via cyclic magma pressurisation. Earth Planet Sci Lett 349:231–239. doi:10.1016/j.epsl.2012.07.003

Benson PM, Vinciguerra S, Meredith PG, Young RP (2008) Laboratory simulation of volcano seismicity. Science 322(5899):249–252

Berryman JG (1992) Effective stress for transport properties of inhomogeneous rocks. J Geophys Res 97(B12):17,409–17,424. doi:10.1029/92JB01593

Biot MA (1941) General theory of three-dimensional consolidation. J Appl Phys 12(2):155–164

Boué A, Lesage P, Cortés G, Valette B, Reyes-Dávila G (2015) Real-time eruption forecasting using the material failure forecast method with a Bayesian approach. Solid Earth, Journal of Geophysical Research

Brantut N, Heap MJ, Meredith PG, Baud P (2013) Time-dependent cracking and brittle creep in crustal rocks: a review. J Struct Geol 52:17–43. doi:10.1016/j.jsg.2013.03.007

Caricchi L, Pommier A, Pistone M, Castro J, Burgisser A, Pergini D (2011) Strain-induced magma outgassing: insights from simple-shear experiments on bubble bearing melts. Bull Volcanol 73:1245–1257. doi:10.1007/s00445-011-0471-2

Chouet BA (1996) Long-period volcano seismicity: its source and use in eruption forecasting. Nature 380:309–316. doi:10.1038/380309a0

Collinson ASD, Neuberg JW (2012) Gas storage, transport and pressure changes in an evolving permeable volcanic edifice. J Volcanol Geoth Res 243–244:1–13. doi:10.1016/j.jvolgeores.2012.06.027

Costa, A., Melnik, O., and Vedeneeva, E. (2007). Thermal effects during magma ascent in conduits. Journal of Geophysical Research: Solid Earth (1978–2012), 112(B12).

Day SJ (1996) Hydrothermal pore fluid and the stability of porous, permeable volcanoes. Q J Geol Soc Lond 111:77–93. doi:10.1144/GSL.SP.1996.110.01.06

De Lauro E, De Martino S, Palo M, Ibáñez JM (2012) Self-sustained oscillations at Volcán de Colima (México) inferred by independent component analysis. Bull Volcanol 74:279–292

Denlinger RP, Hoblitt RP (1999) Cyclic eruptive behavior of silicic volcanoes. Geology 27(5):459–462

Diller K, Clarke AB, Voight B, Neri A (2006) Mechanisms of conduit plug formation: implications for vulcanian explosions. Geophys Res Lett 33:L20302. doi:10.1029/2006GL027391

Donnadieu F, Merle O, Besson J-C (2001) Volcanic edifice stability during cryptodome intrusion. Bull Volcanol 63:61–72. doi:10.1007/s004450000122

Edmonds M, Oppenheimer C, Pyle DM, Herd RA, Thompson G (2003) SO2 emissions from Soufrière Hills Volcano and their relationship to conduit permeability, hydrothermal interaction and outgassing regime. J Volcanol Geoth Res 124:23–43. doi:10.1016/S0377-0273(03)00041-6

Elsworth D, Voight B (1992) Theory of dike intrusion in a saturated porous solid. J Geophys Res: Solid Earth (1978–2012) 97(B6):9105–9117. doi:10.1029/92JB00519

Elsworth D, Voight B, Ouyang Z, Piggott AR (1996) Poroelastic response resulting from magma intrusion, Mechanics of Poroelastic Media. Springer, Netherlands, pp 215–233

Farquharson J, Heap MJ, Varley NR, Baud P, Reuschlé T (2015) Permeability and porosity relationships of edifice-forming andesites: a combined field and laboratory study. J Volcanol Geotherm Res 297:52–68

Faulkner DR, Rutter EH (2001) Can the maintenance of overpressured fluids in large strike-slip fault zones explain their apparent weakness? Geology 29(6):503–506

Gaunt HE, Sammonds PR, Meredith PG, Smith R, Pallister JS (2014) Pathways for degassing during the lava dome eruption of Mount St. Helens 2004–2008. Geology 42(11):947–950. doi:10.1130/G35940.1

Gerst A, Savage MK (2004) Seismic anisotropy beneath Ruapehu Volcano: a possible eruption forecasting tool. Science 306:1543–1547

Giammanco S, Gurrieri S, Valenza M (1998) Anomalous soil CO2 degassing in relation to faults and eruptive fissures on Mount Etna (Sicily, Italy). Bull Volcanol 60(4):252–259

Gudmundsson A (2011) Rock fractures in geological processes. Cambridge University Press, UK

Gudmundsson A, Friese N, Galindo I, Philipp SL (2008) Dike-induced reverse faulting in a graben. Geology 36(2):123–126

Guéguen Y, Palciauskas V (1994) Introduction to the physics of rocks. Princeton University Press, UK

Hagerty MT, Schwartz SY, Garces MA, Protti M (2000) Analysis of seismic and acoustic observations at Arenal Volcano, Costa Rica, 1995–1997. J Volcanol Geotherm Res 101:27–65

Harris AJL, Maciejewski AJH (2000) Thermal surveys of the Vulcano Fossa fumarole field 1994–1999: evidence for fumarole migration and sealing. J Volcan Geotherm Res 102:119–147

Harrington RM, Brodsky EE (2007) Volcanic hybrid earthquakes that are brittle-failure events. Geophys Res Lett 34(6). doi:10.1029/2006GL028714

Heap MJ, Farquharson Y, Baud P, Lavallée Y, Reuschlé T (2015a) Fracture and compaction of andesite in a volcanic edifice. Bull Volcanol 77(6):1–19

Heap MJ, Xu T, Kushnir ARL, Kennedy BM, Chen C-f (2015b) Fracture of magma containing overpressurised pores. Journal of Volcanology and Geothermal Research, Accepted

Heap MJ, Kennedy BM, Pernin N, Jacquemard L, Baud P, Farquharson JI, Dingwell DB (2015c) Mechanical behaviour and failure modes in the Whakaari (White Island volcano) hydrothermal system, New Zealand. J Volcanol Geotherm Res 295:26–42

Heap MJ, Lavallée Y, Petrakova L, Baud P, Reuschlé T, Varley NR, Dingwell DB (2014a) Microstructural controls on the physical and mechanical properties of edifice-forming andesites at Volcán de Colima, Mexico. J. Geophys. Res. Solid Earth 119. doi: 10.1002/2013JB010521.

Heap, MJ., Baud, P., Meredith, P. G., Bell, A. F., and Main, I. G. (2009). Time-dependent brittle creep in Darley Dale sandstone. J Geophys Res Solid Earth (1978–2012), 114(B7).

Heap MJ, Baud P, Meredith PG, Vinciguerra S, Reuschlé T (2014b) The permeability and elastic moduli of tuff from Campi Flegrei, Italy: implications for ground deformation modelling. Solid Earth 5:25–44

Heiken G, Wohletz K, Eichelberger JC (1988) Fracture fillings and intrusive pyroclasts, Inyo Domes, California. J Geophys Res 93:4335–4350

Heiligmann M, Stix J, Williams-Jones G, Lollar BS, Garzón VG (1997) Distal degassing of radon and carbon dioxide on Galeras Volcano, Colombia. J Volcanol Geotherm Res 77(1):267–283

Heimisson ER, Einarsson P, Sigmundsson F, Brandsdóttir B (2015) Kilometer-scale Kaiser effect identified in Krafla Volcano. Iceland, Geophysical Research Letters

Hubbert MK, Rubey WW (1959) Role of fluid pressure in mechanics of overthrust faulting: I. Mechanics of fluid-filled porous solids and its application to overthrust faulting. Geo Soc Am Bull 70:115–166. doi:10.1130/0016-7606(1959)70[167:ROFPIM]2.0.CO;2

Hurwitz S, Johnston MJ (2003) Groundwater level changes in a deep well in response to a magma intrusion event on Kilauea Volcano, Hawai'i. Geophys Res Lett 30:22. doi:10.1029/2003GL018676

Hutchison W, Varley N, Pyle DM, Mather TA (2013) In: Pyle DL, Mather TA (eds) Remote sensing of volcanoes & volcanic processes: integrating observation & modelling. Geological Society, London, pp 203–228

James MR, Lane SJ, Chouet B, Gilbert JS (2004) Pressure changes associated with the ascent and bursting of gas slugs in liquid-filled vertical and inclined conduits. J Volcanol Geoth Res 129:61–82. doi:10.1016/S0377-0273(03)00232-4

James MR, Varley N (2012) Identification of structural controls in an active lava dome with high resolution DEMs: Volcán de Colima. Mexico Geophys Re Lett 39:L22303. doi:10.1029/2012GL054245

Jaupart C (1998) Gas loss from magmas through conduit walls during eruption. J Geol Soc 145:73–90

Johnson JB, Lees JM (2000) Plugs and chugs—seismic and acoustic observations of outgassing explosions at Karymsky, Russia and Sangay. Ecuador J Volcanol Geoth Res 101:67–82. doi:10.1016/S0377-0273(00)00164-5

Johnson PA, McEvilly TV (1995) Parkfield seismicity: fluid-driven? J Geophys Res 100:12937–12950. doi:10.1029/95JB00474

Jousset P, Budi-Santoso A, Jolly AD, Boichu M, Surono DS, Sumarti S, Hidayati S, Thierry P (2013) Signs of magma ascent in LP and VLP seismic events and link to outgassing: an example from the 2010 explosive eruption at Merapi Volcano. Indonesia J Volcanol Geoth Res 261:171–192. doi:10.1016/j.jvolgeores.2013.03.014

Kaiser L (1953) Erkenntnisse und folgerungen aus der messung von geräuschen bei zugbeanspruchung von metallischen werkstoffen. Arch Eisenhüttenwesen 24:43–45

Kendrick JE, Smith R, Sammonds P, Meredith PG, Dainty M, Pallister JS (2013) The influence of thermal and cyclic stressing on the strength of rocks from Mount St. Helens, Washington. Bull Volcanol 75(7):1–12

Kennedy LA, Russell JK, Nelles E (2009) Origins of Mount St. Helens cataclasites: experimental insights. Am Mineral 94:995–1004

Knapp RB, Knight JE (1977) Differential thermal expansion of pore fluids: fracture propagation and microearthquake production in hot pluton environments. J Geophys Res 82(17):2515–2522

Kolzenburg S, Heap MJ, Lavallée RJK, Meredith PG, Dingwell DB (2012) Strength and permeability recovery of tuffisite-bearing andesite. Solid Earth 3:191–198. doi:10.5194/se-3-191-2012

Kranz RL, Scholz CH (1977) Critical dilatant volume of rocks at the onset of tertiary creep. J Geophys Res 82(30):4893–4898

Kumagai H, Chouet BA, Nakano M (2002) Temporal evolution of a hydrothermal system in Kusasutsu-Shirane Volcano, Japan, inferred from the complex frequencies of long-period events. J Geophys Res 107:B11–B2301. doi:10.1029/2001JB000653

Lagmay AMF, de Vries BVW, Kerle N, Pyle DM (2000) Volcano instability induced by strike-slip faulting. Bull Volcanol 62(4–5):331–346

Lahr JC, Chouet BA, Stephens CD, Power JA, Page RA (1994) Earthquake classification, location, and error analysis in a volcanic environment: implications for the magmatic system of the 1989–1990 eruptions at redoubt volcano. Alaska J Volcanol Geoth Res 62:137–151. doi:10.1016/0377-0273(94)90031-0

Lavallée Y, Benson PM, Heap MJ, Flaws A, Hess K-U, Dingwell DB (2011) Volcanic conduit failure as a trigger to magma fragmentation. Bull Volcanol 74:11–13

Lavallée Y, Benson PM, Heap MJ, Hess KU, Flaws A, Schillinger B, Dingwell DB (2013) Reconstructing magma failure and the degassing network of dome-building eruptions. Geology 41(4):515–518. doi:10.1130/G33948.1

Lavallée Y, Heap MJ, Kueppers U, Kendrick J, Dingwell DB (2016) The fragility of Volcán de Colima—a material constraint. In: Varley N, Komorowski J-C (eds) Volcán de Colima: managing the threat. Active Volcanoes of the World. Springer, New York, **ISBN 978-3-642-25910-4 (In Press)**

Lavrov A (2003) The Kaiser effect in rocks: principals and stress estimation techniques. Int J Rock Mech Min Sci 40:151–171

Lensky NG, Navon O, Lyakhovsky V (2004) Bubble growth during decompression of magma: experimental and theoretical investigation. J Volcanol Geoth Res 129:7–22. doi:10.1016/S0377-0273(03)00229-4

Loaiza S, Fortin J, Schubnel A, Gueguen Y, Vinciguerra S, Moreira M (2012) Mechanical behavior and localized failure modes in a porous basalt from the Azores. Geophys Res Lett 39(19)

Lockner D (1993) The role of acoustic emission in the study of rock fracture. Int J Rock Mech Min Sci 30:883–899. doi:10.1016/0148-9062(93)90041-B

Luhr JF (2002) Petrology and geochemistry of the 1991 and 1998–1999 lava flows from Volcán de Colima, México: implications for the end of the current eruptive cycle. J Volcanol Geoth Res 117:169–194. doi:10.1016/S0377-0273(02)00243-3

Melnik O, Barmin AA, Sparks RSJ (2005) Dynamics of magma flow inside volcanic conduits with bubble overpressure buildup and gas loss through permeable magma. J Volcanol Geotherm Res 143(1):53–68

Michaut C, Ricard Y, Bercovici D, Sparks RSJ (2013) Eruption cyclicity at silicic volcanoes potentially caused by magmatic gas waves. Nat Geosci 6(10):856–860

Mueller SB, Varley NR, Kueppers U, Lesage P, Reyes-Davila GA, Dingwell DB (2013) Quantification of magma ascent rate through rockfall monitoring at the growing/collapsing lava dome of Volcan de Colima, Mexico. Solid Earth. 4/ 201–213. doi: 10.5194:se-4-201-2013.

Mueller S, Scheu B, Kueppers U, Spieler O, Richard D, Dingwell DB (2011) The porosity of pyroclasts as an indicator of volcanic explosivity. J Volcanol Geotherm Res 203(3):168–174

Nara Y, Meredith PG, Yoneda T, Kaneko K (2011) Influence of macro-fractures and micro-fractures on permeability and elastic wave velocities in basalt at elevated pressure. Tectonophysics 503(1):52–59

Neuberg J (2000) Characteristics and causes of shallow seismicity in andesite volcanoes. Philosophical Transactions of the Royal Society of London. Series A Math Phys Eng Sci 358(1770):1533–1546

Neuberg JW, Tuffen H, Collier L, Green D, Powell T, Dingwell D (2006) The trigger mechanism of low-frequency earthquakes on Montserrat. J Volcanol Geotherm Res 153(1):37–50

Newhall CG, Albano SE, Matsumoto N, Sandoval T (2001) Roles of groundwater in volcanic unrest. J Geol Soc Phil 56:69–84

Nicholson EJ, Mather TA, Pyle DM, Odbert HM, Christopher T (2013) Cyclical patterns in volcanic degassing revealed by SO 2 flux timeseries analysis: an application to Soufrière Hills Volcano, Montserrat. Earth Planet Sci Lett 375:209–221

Nishi Y, Sherburn S, Scott SJ, Sugihara M (1996) High-frequency earthquakes at White Island volcano, New Zealand: insights into the shallow structure of a volcano hydrothermal system. J Volcanol Geoth Res 72:183–197. doi:10.1016/0377-0273(96)00005-4

Ougier-Simonin A, Zhu W (2013) Effects of pore fluid pressure on slip behaviors: an experimental study. Geophys Res Lett 40:2619–2624. doi:10.1002/grl.50543

Palo M, Ibanez JM, Cisneros M, Breton M, Del Pezzo E, Ocana E, Orozco-Rojas J, Posadas AM (2009) Analysis of the seismic wavefield properties of volcanic explosions at Volcan de Colima, Mexico: insights into the source mechanism. Geophys J Int 177: 1383–1398. doi:10.1111/j.1365-246X.2009.04134.x

Paterson MS, Wong T-f (2005) Experimental rock deformation—the brittle field, 2nd edn. Springer, New York

Petersen T, Caplan-Auerbach J, McNutt SR (2006) Sustained long period seismicity at Shishaldin Volcano, Alaska. J Volcanol Geotherm Res 151:365–381

Petrosino S, Cusano P, La Rocca M, Galluzzo D, Orozco-Rojas J, Bretón M, Ibañez J, Del Pezzo E (2011) Source location of long period seismicity at Volcàn de Colima. México Bull Volcanol 73:887–898

Plail M, Edmonds M, Humphreys M, Barclay J, Herd RA (2014) Geochemical evidence for relict degassing pathways preserved in andesite. Earth Plan Sci Let 386:21–33. doi:10.1016/j.epsl.2013.10.044

Power JA, Stihler SD, White RA, Moran SC (2004) Observations of deep long-period (DLP) seismic events beneath Aleutian arc volcanoes; 1989–2002. J Volcanol Geotherm Res 138(3):243–266

Reid ME, Christian SB, Brien DL (2000) Gravitational stability of three-dimensional stratovolcano edifices. J Geophys Res 105:6043–6056. doi:10.1029/1999JB900310

Roman DC, Moran SC, Power JA, Cashman KV (2004) Temporal and spatial variation of local stress fields before and after the 1992 eruptions of Crater Peak Vent, Mount Spurr Volcano, Alaska. Bull Seismol Soc Am 94:2366–2379

Rubey WW, Hubbert MK (1959) Role of fluid pressure in mechanics of overthrust faulting: II. Overthrust belt in geosynclinal area of western Wyoming in light of fluid-pressure hypothesis. Geo Soc Am Bull 70:167–206. doi:10.1130/0016-7606(1959)70[167:ROFPIM]2.0.CO;2

Rust AC, Cashman KV, Wallace PJ (2004) Magma degassing buffered by vapor flow through brecciated conduit margins. Geology 32(4): 349–352

Savov IP, Luhr JF, Navarro-Ochoa C (2008) Petrology and geochemistry of lava and ash erupted from Volcán Colima, Mexico, during 1998–2005. J Volcanol Geoth Res 174:241–256. doi:10.1016/j.jvolgeores.2008.02.007

Shibata T, Akita F (2001) Precursory changes in well water level prior to the March, 2000 eruption of Usu Volcano, Japan. Geophys Res Lett 28(9):1799–1802. doi:10.1029/2000GL012467

Shiina T, Nakajima J, Matsuzawa T (2013) Seismic evidence for high pore pressures in the oceanic crust: implications for fluid-related embrittlement. Geophys Res Lett 40(10):2006–2010

Shields JK, Mader HM, Pistone M, Caricchi L, Floess D, Putlitz B (2014) Strain-induced outgassing of three-phase magmas during simple shear. J Geophys Res Solid Earth 119(9):6936–6957. doi:10.1002/2014JB011111

Sigurdsson O (1982) Analysis of pressure pulses resulting from volcanic activity in the vicinity of a well, M.S. Thesis. University of Oklahoma, Norman, p 75

Sisson TW, Power JA (2013) Deep-crustal seismicity in volcanic regions by fluid-enhanced wallrock embrittlement. American Geophysical Union, Fall Meeting 2013, abstract #V13B-2616.

Sisson TW, Bacon CR (1999) Gas-driven filter pressing in magmas. Geology 27(7):613–616

Stevenson JA, Varley N (2008) Fumarole monitoring with a handheld infrared camera: Volcán de Colima, Mexico, 2006–2007. J Volcanol Geotherm Res 177(4):911–924

Strehlow K, Gottsmann JH, Rust AC (2015) Poroelastic responses of confined aquifers to subsurface strain changes and their use for volcano monitoring. Solid Earth Discuss 7:1673–1729. doi:10.5194/sed-7-1673-2015

Taisne B, Juapart C (2008) Magma outgassing and intermittent lava dome growth. Geophys. Res. Lett. 35: L20310. doi: :10.1029/2008GL035432.

Taran Y, Gavilanes JC, Cortés A, Armienta MA (2000) Chemical precursors to the 1998–1999 eruption of Colima Volcano, Mexico. Revista mexicana de ciencias geológicas 17(2):111–124

Terzaghi KV (1923) Die Berechnung der Durchlässigkeitsziffer des Tones aus dem Verlauf der hydrodynamischen Spannungserscheinungen. [The calculation of the permeability coefficient of clay from the variation of hydrodynamic stress phenomena]. Sitzungsberichte der Akademie der Wissenschaften in Wien, Mathematisch-Naturwissenschaftliche Klasse. Abteilung IIa 132: 125–138

Thomas ME, Neuberg J (2012) What makes a volcano tick—a first explanation of deep multiple seismic sources in ascending magma. Geology 40:351–354. doi:10.1130/G32868.1

Thomas ME, Petford N, Bromhead EN (2004) The effect of internal gas pressurization on volcanic edifice stability: evolution towards a critical state. Terra Nova 16(5):312–317

Varley NR, Taran Y (2003) Degassing processes of Popocatépetl and Volcán de Colima, Mexico. Geol Soc Lond, Spec Publ 213(1): 263–280

Varley N, Arámbula-Mendoza R, Sanderson R, Stevenson J (2010) Generation of Vulcanian activity and long-period seismicity at Volcán de Colima, Mexico. J Volcanol Geoth Res 198(1–2):45–56. doi:10.1016/j.jvolgeores.2010.08.009

Vinciguerra S, Meredith PG, Hazzard J (2004) Experimental and modeling study of fluid pressure-driven fractures in Darley Dale sandstone. Geophys Res Lett 31:L09609. doi:10.1029/2004GL019638

Voight B, Elsworth D (1997) Failure of volcano slopes. Geotechnique 47: 1–31. doi:10.1680/geot.1997.47.1.1

Voight B, Sparks RJS, Miller AD, Stewart RC, Hoblitt RP, Clarke A, Ewart J, Aspinall WP, Baptie B, Calder ES, Cole P, Druitt TH, Hartford C, Herd RA, Jackson P, Lejeune AM, Lockhart AB, Loughlin SC, Luckett R, Lynch L, Norton GE, Robertson R, Watson IM, Watts R, Young SR (1999) Magma flow instability and cyclic activity at Soufriere Hills Volcano, Montserrat, British West Indies. Science 283:1138–1142. doi:10.1126/science.283.5405.1138

Wang HF (2000) Theory of linear poroelasticity with applications to geomechanics and hydrogeology. Princeton Univ, Press, Princeton, N. J

Watson IM, Oppenheimer C, Voight B, Francis PW, Clarke A, Stix J, Staff MVO (2000) The relationship between degassing and ground deformation at Soufriere Hills Volcano, Montserrat. J Volcanol Geoth Res 98(1):117–126

Watters RJ, Zimbelman DR, Bowman SD, Crowley JK (2000) Rock mass strength assessment and significance to edifice stability, Mount Rainier and Mount Hood, Cascade Range Volcanoes. Pure Appl Geophys 157:957–976. doi:10.1007/s000240050012

Wong T-f, Baud P (2012) The brittle-ductile transition in porous rock: a review. J Struct Geol 44:25–53. doi:10.1016/j.jsg.2012.07.010

Wong T-f, David C, Zhu W (1997) The transition from brittle faulting to cataclastic flow in porous sandstones: mechanical deformation. Solid Earth 102:3009–3025. doi:10.1029/96JB03281

Woods AW, Koyaguchi T (1994) Transitions between explosive and effusive eruptions of silicic magmas. Nature 370:641–644. doi:10.1038/370641a0

Yokoo A, Iguchi M, Tameguri T, Yamamoto K (2013) Processes prior to outbursts of vulcanian eruption at Showa Crater of Sakurajima Volcano. Bull Volcanol Soc Japan 58:163–181

Young NK, Gottsmann J (2015) Shallow crustal mechanics from volumetric strain data: Insights from Soufrière Hills Volcano, Montserrat. J Geophys Res: Solid Earth 120(3):1559–1571

Zhu W, Baud P, T-f W (2010) Micromechanics of cataclastic pore collapse in limestone. J Geophys Res Solid Earth 115:B4. doi:10.1029/2009JB006610

Zhu W, Baud P, Vinciguerra S, Wong TF (2011) Micromechanics of brittle faulting and cataclastic flow in Alban Hills tuff. J Geophys Res 116:B06209. doi:10.01029/02010JB008046